Scan to know paper details and
author's profile

Rheological Evidence for a Probable Rarefied Crust and Fracture Characterization under Northern Harrat Rahat, Sw Saudi Arabia: Its Significance for Geothermal Prospects

Manoj Mukhopadhyay, Basab Mukhopadhyay, Saad Mogren & Elkhedr Ibrahim

PNG University of Technology

ABSTRACT

We analysed the geothermal potential in the Northern Harrat Rahat (NHR), SW Saudi Arabia, where, a 'Low-Gravity-Zone' (LGZ) follows the eastern vent axis and also corresponds to a Low Resistive Zone (LRZ) at 10 to 15 km depth. Anomalous crustal rheological parameters (Vp, Vp/Vs, Density, Poisson's ratio, Young's modulus and Acoustic-Impedance) are noticed on 2.5 km depth-slices underlying the LRZ which are based on receiver-function results from 13 seismic stations distributed within an area of 120 x 128 km^2. Based on these, we inspect crustal rheology under an ENE-WSW traverse taken across the LGZ that unravels finer details of a Low Velocity Zone (LVZ), a Low Density Zone (LDZ), and Low Poisson ratio (σ) and Young's modulus (E) zones in the depth direction over a lateral extent of 120 km at depths between 5 and 17.5 km. Further down, (i) the lower extent of LVZ and LDZ dips eastward from 17.5 to 25 km, suggesting a rarefied crust underneath, and (ii) both Vp and density depth sections illustrate appreciable gradient as they increase from east and west towards the central area beneath the REF seismic stations RH01 and RH14.

Keywords: northern harrat rahat, transitional crust, elastic constants, rheological properties, low-velocity and density zone, geothermal favorability.

Classification: LCC Code: QE509

Language: English

Great Britain
Journals Press

LJP Copyright ID: 925614
Print ISSN: 2631-8490
Online ISSN: 2631-8504

London Journal of Research in Science: Natural & Formal

Volume 25 | Issue 2 | Compilation 1.0

Rheological Evidence for a Probable Rarefied Crust and Fracture Characterization under Northern Harrat Rahat, Sw Saudi Arabia: Its Significance for Geothermal Prospects

Manoj Mukhopadhyay[α], Basab Mukhopadhyay[σ], Saad Mogren[ρ] & Elkhedr Ibrahim[ꙍ]

ABSTRACT

We analysed the geothermal potential in the Northern Harrat Rahat (NHR), SW Saudi Arabia, where, a 'Low-Gravity-Zone' (LGZ) follows the eastern vent axis and also corresponds to a Low Resistive Zone (LRZ) at 10 to 15 km depth. Anomalous crustal rheological parameters (Vp, Vp/Vs, Density, Poisson's ratio, Young's modulus and Acoustic-Impedance) are noticed on 2.5 km depth-slices underlying the LRZ which are based on receiver-function results from 13 seismic stations distributed within an area of 120 x 128 km^2. Based on these, we inspect crustal rheology under an ENE-WSW traverse taken across the LGZ that unravels finer details of a Low Velocity Zone (LVZ), a Low Density Zone (LDZ), and Low Poisson ratio (σ) and Young's modulus (E) zones in the depth direction over a lateral extent of 120 km at depths between 5 and 17.5 km. Further down, (i) the lower extent of LVZ and LDZ dips eastward from 17.5 to 25 km, suggesting a rarefied crust underneath, and (ii) both Vp and density depth sections illustrate appreciable gradient as they increase from east and west towards the central area beneath the REF seismic stations RH01 and RH14. The LVZ, LDZ and Low Poisson Ratio (σ) and Young's Modulus (E) zones under NHR probably owe its origin to a raised geotherm in fractured crust that alters the crustal rheology and shows correspondence to vent axes. Compartmentalization of geophysical properties by orthogonal fractures/faults is used to propose a probable geologic model of heat transfer in the NHR.

Keywords: northern harrat rahat, transitional crust, elastic constants, rheological properties, low-velocity and density zone, geothermal favorability.

Author α σ: PNG University of Technology, Lae, Morobe Province, Papua New Guinea.
σ: Mission III, Geological Survey of India, 29 J. L. Nehru Road, Kolkata – 700016, India.
ρ: King Saud University, P.O. Box 2455, Riyadh 11451, Kingdom of Saudi Arabia.
ꙍ: King Saud University, P.O. Box 2455, Riyadh 11451, Kingdom of Saudi Arabia.

I. INTRODUCTION

The Arabian Shield along the Red Sea Margin (AS-RSM) in SW Saudi Arabia (Figure 1) is tectonically active. It has an average width of 150 km from Red Sea coast and formed by three distinct morphological units: (i) the low-lying coastal plains of median width of 40 km that sustain an elevation up to 100 m, (ii) further inland appears the foothills of the Hijaz-Asir Escarpment Zone (HAEZ), having elevation nearly 500 m and beyond which, (iii) the HAEZ steeply rises to an altitude of 3 km. The area between the shoreline and the HAEZ is occupied irregularly in a wide strip by the basaltic fields (also called harrats) (Brown, 1980). The dominant NNW alignment of the volcanic fields sub-parallel to the regional Red Sea axis were produced by magmatic activity triggered by lithospheric extension. Seismic studies using broadband stations (Tang et al., 2016, 2019) and IRIS seismic profiles (Gettings et al., 1986) identified a low-velocity upper mantle. This low-velocity upper mantle is presumably sourced the magma in the basaltic fields and has a connection with the Afar plume activity (Chang et al., 2011; Lim et al., 2020; Kaviani et al., 2020; Mukhopadhyay et al., 2022). The intrusive and extrusive magmatic phases that occurred during Tertiary time in SW Saudi Arabia are recognized as the final tectono-magnetic events in the study area (Bohannon, 1989). The AS-RSM is segregated by many regional sutures and faults of different ages (Stern & Johnson, 2010, 2019) and divided AS-RSM into three broad geologic divisions; North Red Sea Margin (NRSM), Central Red Sea Margin including the Jeddah Terrane (CRSM & JT), and South Red Sea Margin (SRSM). However, such divisions are mainly speculated on geological grounds rather than concrete geophysical signatures. The large-scale volcanism along the shield edge in SW Saudi Arabia has presumably altered the elastic constants of crustal rocks. A chronicle in the evolution of the geological framework in the region is: (i) the crust has undergone large-scale extension, (ii) the crust experienced extensive regional volcanism to form the harrats, (iii) non-uniform distribution of volcanic fields; the volcanism is conspicuously absent for 400 km in the central part of AS-RSM, and (iv) consequently, there are expected differences in lithology between the upper and lower crust along such discontinuous volcanic belts spread across the region.

The seismic anisotropy in the AS-RSM transitional crust reveals that the rheological character of the crust underneath the AS-RSM is heterogenous. Here the elastic properties vary both laterally and vertically, exhibiting sharp changes between the magma-infested crustal columns. Seismic attributes (wavelet phases and amplitudes) are related to physical properties of the imaged crustal rocks such as Vp, density (ρ), Poisson's ratio (σ), and acoustic-impedance (AI) etc., as they provide meaningful data for an insight to geothermal prospectivity. It is conjectured that "a lack of magmatic activity does not necessarily imply a lack of geothermal systems" (IGA Service GmbH, 2014). Often deep crustal faults and crust-penetrative fracture zones can also transport heat in a thinned crust like the AS-RSM. Geophysical methods, in particular, seismic, magneto-telluric, and gravity have found wide applications in the search of geothermal systems even within a deep crust (Heise et al., 2007; IGA Services GmbH, 2014).

Geothermal productivity at the AS-RSM in Saudi Arabia has gained importance mostly during the last four decades. The prospectivity is distributed amongst its petrographic divisions (Demange, 1984; Al-Dayel, 1988). This happened mainly because of factors like the uplifted Moho at the extensional margin, high-temperature gradient, enhanced heat flow regime under the basaltic harrats, fractured crust, faults and vent axes (refer below). One such recent publication dealt with the 'geothermal favorability map' for Saudi Arabia where the authors integrated the relevant spatial data on Curie depth, temperature gradient, heat flow, fault density, volcanic field density, and seismic event density (Aboud et al., 2021). The Harrat Rahat (marked as 7 in Figure 1) has a near-surface geothermal magmatic system and was investigated by Aboud et al. (2022, 2023) using the MT survey and gravity–magnetic data. The Northern Harrat Rahat (NHR), the northernmost part of Harrat Rahat, presumably has more geothermal potential. In the present study, we investigate the probable correspondence between the crustal rheological parameters and gravity for NHR and try to locate its potential geothermal zones.

Several site-specific variables that are regarded as quite characteristic of geothermal systems are (a) the mechanical properties of rocks, (b) the nature and depth of the heat source, whether magmatic or non-magmatic; (c) distribution of permeability and porosity; (d) the dominant heat transfer mechanism, whether convection or conduction; (e) chemistry of fluid/rock; and (f) fluid recharge rate/source (Chapter 2 in IGA Service GmbH, 2014). Owing to constraints on the data availability, the scope of the present study is confined to only the areas under (a) and (b). Here our objectives are four folds: (i) to present and analyze the rheological parameters for NHR based on the available REF results, (ii) to infer the probable composition of rock prevalent in the upper and lower crust underlying their respective areas for NHR, (iii) to interpret the gravity anomaly mapped over the NHR, by taking a cue from both the REF results as well the MT survey results which have detected a Low Resistivity Zone

(LRZ) at the mid-crust underlying the NHR, and (iv) integrate these results to examine their applicability in gaining an insight into the geothermal system under NHR.

II. GEOLOGY OF NORTHERN HARRAT RAHAT (NHR)

The Harrat Rahat (marked as 7 in Figure 1) covering ~20,000 km^2 area is the major volcanic field in western Saudi Arabia whose characteristic features are reviewed here for ready reference to the readers. The volcanic field is nearly 300 km long and has a maximum width of ~ 75 km (Camp & Roobol, 1989, 1991). Actually, four volcanic fields together constitute the Harrat Rahat, namely; Harrat Ar Rukhq, Harrat Turrah, Harrat Bani Abdullah, and Harrat Rashid from south to north. The northernmost volcanic field is the Harrat Rashid / Harrat Al-Madinah / Northern Harrat Rahat (NHR) (Figure 2). Studies by Down et al (2028, 2019) provide an initial estimate on the volumetric percentage of the various basalts erupted within them: Harrat Rahat contains majority as tholeiitic basalt (~62%), followed by alkali basalt (~21%), hawaite (~13%), and mugearite, benmoreite, trachyte (~4%) in diminishing proportion, where the axial part of the field is significantly occupied by a large number of vents containing mugearite and hawaite. In an earlier study, Brown (1980) had also identified three ages of volcanic rocks: (i) basaltic flow of the Tertiary age, (ii) basaltic flow of the Tertiary and Quaternary ages, and (iii) basaltic flow of the Holocene age. It is of interest to note that the identified rocks have prevalent mantle affinity (Murcia et al., 2016).

In NHR, the eruption is through fissures, tuff ridges, shields and pyroclastic cones. The last known eruptive event occurred near Al Madinah at 1256 AD (Camp et al., 1987; Kereszturi et al., 2016). The identified 900+ volcanic vents (Downs et al., 2019) are aligned along two prominent vent axes, western and eastern, with a separation of nearly 10 km in between having a structural trend of N10°W to N25°W (Runge et al., 2014, 2015) (Figure 2). Field mapping by Downs et al. (2018 and 2019) demonstrate identifiable sequences in eruption and subsequent compositional changes associated with it as a part of evolutionary process in NHR. Their sequence being: (i) Tholeiitic basalts with minor amount of alkali basalts erupted in the first phase, (ii) in Pliocene period, the dominant eruptive phase is alkali basalts, and (iii) since the Pleistocene, alkali basalts are accompanying with hawaiite, mugearite, Benmoreite, and trachyte. The flow of the lava flow is rather fast and even reached 100 km from the vent or eruption side in the downslope direction. From the 10 – 15% increase of shear-wave velocity between 15 and 25 km depth, the interface between the andesitic upper crust and the mafic lower crust was identified in the Arabian Shield (Civilini et al., 2019). The average velocities of the upper and lower crust below Harrat Rahat were estimated through Rayleigh waves as 3.64 and 3.95 km/s, and using Love waves as 3.53 and 4.16 km/s (Civilini et al., 2019). From the above analysis, Civilini et al., (2019) concluded that a crustal magma chamber is absent in the region. Hence, it may be prudent to infer from all other evidence cited above that the magma is coming from a deeper source, probably from the elevated Moho region or from the upper mantle. Due to high thermal flow from the source region, high density of structural and fracture planes within crust and suitable fractured eruptive rock types present, the NHR possess a good geothermal potential. In this regard, the readers are referred to a recent compilation on the subject by Al-Amri et al. (2020).

III. MATERIALS AND METHODS

REF data for the 13 numbers of seismic stations (RH01 to RH11, RH13 to RH15) located on NHR (base data: location of station, Vp, Vs, Vp/Vs along 2.5 km depth, Moho depth) are extracted from Tang et al. (2016, 2019) up to a depth of 40 km with a depth interval of 2.5 km. These data are used here to compute the rheological constants (Density (ρ), Lame's First Constant (λ), Shear Modulus (μ), Poisson's Ratio (σ), Young's Modulus (E), Bulk Modulus (K) and Acoustic-Impedance (AI)) using the following equations for the underlying crust. The results are tabulated (Table 1).

The following equations are used for calculation (Brocher, 2005; Telford et al., 1976; Anderson,1989), where V_P is the P wave velocity and V_S is the S wave velocity.

$$\rho = 1.6612V_p – 0.4721V_p^2 + 0.0671V_p^3 - 0.0043V_p^4 + 0.000106V_p^5 \quad (1)$$

$$\lambda = \rho (V_P^2 – 2V_S^2) \quad (2)$$

$$\mu = Vs^2\rho \quad (3)$$

$$K = \lambda + 2/3(\mu) \quad (4)$$

$$E = \mu(3\lambda+2\mu) / (\lambda+ \mu) \quad (5)$$

$$\sigma = 0.8835 – 0.315V_p + 0.0491V_p^2 – 0.0024V_p^3 \quad (6)$$

$$AI = V_p{}^*\rho \quad (7)$$

The crustal thickness for upper and lower crust for the 13 seismic stations located on NHR are taken from Tang et al. (2016, 2019). We have computed the average values of all rheological parameters based on the thickness data of upper and lower crust. The results are tabulated (Table 2).

IV. RESULTS

4.1. General relationship between the rheological parameters in NHR

The primary features of the rheological parameters and their mutual relationships for NHR up to a depth of 40 km (Table 1) is discussed below.

(i) The regression relationship between Vp and Vs is linear and positive, following the regression equation $Vs = 0.5714Vp + 0.0001$ ($R^2 = 1$). No relationship can be established between Vp and Vp/Vs. The relationship between Vp and density (ρ) is linear and positive where $\rho = 0.2459Vp + 1.2443$ ($R^2 = 0.985$). The regression relation between Vs and density (ρ) is also linear and positive with equation $\rho = 0.4303Vs + 1.2443$ ($R^2 = 0.985$).

(ii) Poisson's ratio (σ) usually corresponds to rock deformation developed by static or dynamic stresses at crustal depth. Here we examine the correlation of σ with other relevant elastic properties like; Vp, Vs, Vp/Vs and ρ. The relationship between Vp and σ is linear and positive, $\sigma = 0.0164\ Vp + 0.1451$ ($R^2 = 0.968$). The Poisson's ratio attains a value of 0.25 at mid-crustal depth underneath the NHR. The regression relationship between Vs and σ follows a linear and negative pattern, $\sigma = 0.0287\ Vs – 0.1451$ ($R^2 = 0.968$). No relationship is seen between Vp/Vs and σ, whereas, the relation between ρ and σ is linear and positive: $\sigma = 0.0671\rho + 0.0613$ ($R^2 = 0.983$).

(iii) A linear relationship is demonstrated by the λ and Vp, $\lambda = 16.28Vp – 63.596$ ($R^2 = 0.983$). The regression relation between Vs and λ is also found to be linear and negative, $\lambda = 28.491Vs – 63.6$ ($R^2 = 0.983$). The relationship between μ and λ is distinctly linear and positive, $\lambda = 0.9411\ \mu + 0.0027$ ($R^2 = 1$). The same is true for the relationship between μ and ρ for NHR, $\rho = 0.0011\mu + 0.2092$ ($R^2 = 0.988$). Likewise, the relationship between ρ and λ is linear and negative, $\lambda = 66.3\rho – 146.23$ ($R^2 = 0.999$).

4.2. Rheological properties and inferred crustal rocks under NHR

The variation in Vp/Vs ratio on a regional scale indicates a change in crustal composition. In the crust, an increase in Vp/Vs with depth is directly proportional to a decrease in silica content. In the North American craton, Vp/Vs variation is utilized to map the lithological variation in the crust with depth in two crustal provinces: Grenville Province (average Vp/Vs = 1.81) and the Appalachian Province (average Vp/Vs = 1.73) (Musacchio et al., 1997). Vp/Vs for NHR ranges from 1.740 to 1.750 in the upper crust and from 1.749 to 1.750 in the lower crust. The Vp versus Vp/Vs relationship is used to identify the rock compositions at 2 and 10 Kba pressures respectively (Musacchio et al., 1997). We infer that the rock composition is mostly uniform and felsic in the upper crust under 2 Kba pressure and mafic in the lower crust under 10 Kba pressure.

The distribution of Poisson's Ratio (σ) values has been used by workers to infer the probable rock types mostly prevalent in the upper and lower crust (Gercek, 2007). The σ value in the upper crust ranges from 0.2357 – 0.2495 and that for the lower crust is from 0.2422 to 0.2748, their corresponding plot on the Gercek diagram infers the prevalence of granodiorite to diorite in the upper crust to a gabbroic lower crust (Figure 3), where the rocks are probably less hydrous (cf. Christensen, 1996).

Ji et al. (2010) have reported a comprehensive database demonstrating the relationships between Vp, Vs and ρ for crustal rocks at 600 MPa based on 401 samples (amphibolite (N=31), peridotite (N=38), serpentinized peridotite (N=15), eclogite (N=54), gabbro, diabase, mafic gneiss and mafic granulite (N=118), granodiorite, diorite, felsic gneiss, intermediate gneiss and meta-sediments (N=145), anorthosite (N=8), basalt (N=21) and limestone/marble (N=29)). When we compare and correlate the plots of Vp – λ, Vs – λ, and ρ - λ of the present study on NHR and that to the regression plot and rock types published in Ji et al. (2010) (Figure 4). We infer a felsic upper crust (with felsic to intermediate gneiss and diorite) and a mafic lower crust (mafic gneiss, amphibolite, gabbro and diabase rocks) underlying the NHR.

The Acoustic Impedance (AI) in rocks when plotted against the depth has proven to indicate the presence of a possible seismic discontinuity in the continental crust. Diaferia and Cammarano (2017) have utilized AI for the case of a three-layered crustal model to understand the source of seismic discontinuity in terms of compositional changes that occurred due to the transition of different mineral phases at depths. Accordingly, the average AI values corresponding to a two-layered crust (after Gettings et al., 1986) in the NHR are plotted (Figure 5). Notice that there are distinct shifts in average AI in four zones (A to D, Figure 5) below NHR.

- A rapid change in average AI from surface to 5 km depth (zone A) is attributed to the basaltic flow rocks and diabase dike sheets within silicic crust.
- Change in average AI at 12 km is the junction between the upper and lower crust (Zone B). The upper mostly silicic crust is ~10 – 12 km thick.
- From 12 km to 32 km (zone C) is the lower crust. The rapid change of AI between the upper and lower crust is possibly due to a phase transition of the quartz. The high-temperature gradient in the NHR favours the transition of α quartz to β quartz, plagioclase breakdown and formation of clinopyroxene, which triggers a sudden increase in AI and also Vp/Vs ratio (cf. Rudnick & Gao, 2014; Diaferia & Cammerano, 2017). Here the inferred rock types are gabbro and mafic gneiss.
- Zone D is the lithospheric mantle with possible high-grade mafic granulite and eclogite.

4.3. Rheological variation in the concentric zones around the low resistive zone in NHR

Four concentric circles are visualized circumventing the peak 'Low Resistive Zone' (LRZ, after Aboud et al., 2023) beneath NHR (Figure 6), centered at 24°20'N, 39°50'E. The LRZ is mapped based on the MT survey (Aboud et al., 2023). The radial concentric zones centered at 24°20'N, 39°50'E, denoted as a – d of Figure 6, have respective radii values up to 10, 40, 55 and 100 km and contain 13 REF seismic stations situated in the NHR (source Tang et al., 2019). The NHR is traversed by NW-trending faults/lineaments. The LRZ orients NE are almost orthogonal to the regional tectonic trend. The inverted model given by Aboud et al. (2023) identifies a main magma chamber at 10 – 15 km depth, with very low resistivity in its interior (3 Ωm). The thermal reservoir is estimated to have a large area extent of ~1000 km^2 based on gravity-magnetic data analysis (Aboud et al., 2022). The variation of rheological parameters within the radial zones a - d circumventing the LRZ is analyzed. The upper crust (10 – 15 km thick) has low values of Vp/Vs, density (ρ) and AI within the 10 km zone (Figure 7). The parameters (Vp/Vs, density (ρ) and AI) remain almost constant away from LRZ up to 100 km. Whereas, in the lower crust, an increase in density (ρ) and decrease in Poisson's ratio (σ) is observed away from the LRZ up to 100 km radial distance zone. This is due to the presence of a large magma chamber with more than 1000 km^2 area extent surrounding LRZ, and accompanied by a high heat flow. The LRZ is associated with a distinct lowering in Vp/Vs, ρ, σ and AI-values compared to surrounding seismic stations. This leads us to inspect the rheological variation in 2.5 km depth slices for the crustal columns in the following section.

4.4. Distribution of crustal rheological parameters and gravity in the region of the vent axes of NHR

4.4.1. Contoured Maps of selective rheological parameters in 2.5 and 5 km depth slices

This is undertaken here by presenting contoured maps of selective rheological parameters (Figures 8 and 9). In the 2.5 km depth slice (Figure 8), the parameters [Vp, Vs, Vp/Vs ratio, Density (ρ), Poisson's ratio (σ), and Acoustic Impedance (AI)] show comparatively a broad arcuate low-value zone trending ENE-WSW to N-S below seismic stations RH13, RH1, RH14, RH9 and RH11 (Figure 8). The broad low-value zones recover with comparatively higher values on both sides towards SE and NW (Figure 8). The arcuate anomalous zone of rheological parameters indicates a highly fractured basement with less density and high-temperature melt zones below NHR. Broadly it refers to the properties of the crustal column beneath NHR. We infer that the crustal column is enriched in mafic content, amenable to deform with moderate/less resistance, and changes its volume under high shear-strain conditions produced by magmatic intrusions from the subcrustal level. The contoured maps of the same rheological parameters at 5 km level (Figure 9) show more restricted low value anomalies encompassing three seismic stations (RH01, RH14 and RH15) below NHR and its extension in the northern part up to RH09. The 'Low Resistive Zone' (LRZ) (Aboud et al., 2023) around seismic station RH1 also coincides with low-value zones of all rheological parameters indicating the presence of high-temperature melt within a 5 km depth zone. The restricted nature of Vp and density (ρ) anomalies along the top 5 km in NHR prompted us to analyse its continuation further down depth along a traverse discussed in the following sections.

4.4.2 The Bouguer anomaly and its relationship with low velocity, low density and low resistivity zones in NHR

The Bouguer anomaly map of NHR (Figure 10) is reported by Langenheim (2018); the map is based on terrain-corrected anomaly for 302 gravity stations. Most conspicuous feature present on the B.A. map is an axial gravity low running in NNW-SSE direction through the NHR with flanking gravity highs. The Axial Gravity Low also extends northward over the surrounding Proterozoic basement rocks outside the harrat, suggesting its deep crustal origin (Langenheim et al., 2019). Figure 10 illustrates an intimate correspondence of the Axial Gravity Low with the eastern vent axis, though this correlation is less clear for the western vent.

We further explore the connection between the gravity anomalies with the distribution of four rheological parameters Vp, density, Poisson Ratio (σ) and Young's Modulus (E) to a depth of 40 km along a traverse A-A' perpendicular to the central low gravity zone (see location of A – A' section in Figure 10). The distribution of Vp, density, σ, and E along depth (up to 40 km) for five seismic stations (RH05, RH13, RH01, RH14 and RH02) in the ENE-ESE direction are illustrated along with gravity profile for traverse A-A' (Figures 11 & 12). The zone of low gravity unravels a Low Velocity Zone (LVZ), a Low Density Zone (LDZ), a Low Poisson Ratio (σ) and Young's Modulus (E) zones at crustal depths of

5 to 17.5 km; all these are based on 2.5 km depth slices (Figure 11 & 12). The lower extent of LVZ, LDZ, Low Poisson Ratio (σ) and Young's Modulus (E) zones dips eastward from 17.5 km to 25 km across a lateral extent of 120 km underlying the traverse where gravity low is envisaged for 90 km between RH13 and RH2. This result also implies that the eastern vent axis is more deep-rooted than the western vent axis in NHR. Broadly it refers to the properties of the crustal column which is highly fractured beneath the low gravity zone. The low Poisson Ratio (σ) and Young's Modulus (E) are places where the rocks are hydraulically fractured due to high strain and transmit the heat to raise geotherm (see also Lees and Wu, 2000; Head et al. 2021). The lower crust here is with low silica and high mafic contents, and deforms in moderate/low resistance with volume changes under high-strain produced from intrusions of magmatic dykes from mantle. Thus, the fractured crustal column is dyke-invaded and carries magmatic material through deep-seated faults from a magma chamber probably residing in deep crust. The faults with multiple channels on the upper part of the crustal column produce the LVZ, LRZ (with very low resistivity 3 Ωm in its interior as documented by Aboud et al., 2023) and LDZ. These faults in turn have produced vents on the top surface to outpour basaltic magmas. In this scenario, the vent axes coincide with the low gravity anomaly (Figures 10, 11 and 12). The magma to our understanding is produced by partial melting in the mafic crust and is presumably related to Afar plume activity. We opined earlier also that the gravity axial low zone in NHR is regarded as the probable locale for fractured dyke invaded crust which acts as a feeder zone; where a raised thermal regime heralded gross compositional changes in the lower crust in consequence of crust-mantle interaction (Mogren et al., 2021).

V. DISCUSSION

5.1. Rheological properties, gravity and its relation to the geothermal system in NHR

The tectonically active crust under the Arabian Shield Edge along the Red Sea Margin (AS-RSM) in SW Saudi Arabia has gained attention in recent years due to its geothermal potential. Of particular interest in the region is NHR, where two NNW-trending parallel vent axes separated by a distance of ~10 km are mapped (Figure 2). Earlier studies have reported a prominent LGZ (Figure 10) which follows the eastern vent axis, although this correlation is less clear for the western vent axis. The low gravity zone displays moderate to fair correspondence to a LRZ previously detected by MT surveys under NHR at 10-15 km depth. The average velocities are low for both Raleigh (3.64 -3.95 km/s) and Love (3.53 - 4.16 km/s) waves from the upper to lower crust which supports a low-velocity zone underneath the Large Igneous Province (LIP) in Saudi Arabia.

In the earlier sections, we inspected the LGZ by using the rheological parameters of 13 REF seismic stations data and found that the distribution of average rheological parameters in upper and lower crustal columns does not discriminate the crust underneath the low gravity zone as compared to the surrounding crust out-to-a-radial-zone of 100 km circumventing it. This inference radically improves when the rheological properties are inspected in 2.5 km depth slices for the upper and lower crust as illustrated by a traverse A-A', constrained by five numbers of REF seismic stations, taken in ENE-WSW direction across the LGZ. Here most conspicuously, a LVZ, LDZ, a Low Poisson Ratio (σ) and Young's Modulus (E) zones persist across a lateral extent of 120 km at crustal depths of 5 - 17.5 km. Further down the section, the lower extent of LVZ, LDZ, a Low Poisson Ratio (σ) and Young's Modulus (E) dips eastward from 17.5 km to 25 km, whose overall pattern suggests a rarefied crust underneath the region. The Vp and density in depth section illustrate appreciable gradients as they increase both from east and west towards the central area (situated beneath the seismic stations RH01 and RH14). The envisaged LVZ, LDZ, and Low Poisson Ratio (σ) and Young's Modulus (E) zones for the upper to mid-crust under NHR probably owe its origin to a raised geotherm and highly fractured nature of crust producing alteration in crustal rheology, where the vent axes are reflected on gravity data collected by USGS (Downs et al., 2019).

5.2. Relevance of existing fault systems in NHR and its geothermal favorability

Different approaches have been used in seismic surveys to infer the potentiality of the geothermal fields; examples are the stress-depth distribution (Kusznir et al. 1991), the change in Vp/Vs ratio (Casertano et al., 1980; Kasahara et al., 2020; Lin, 2020; Muluneh et al., 2021) constructed the Yield Strength Envelopes (YSE) to examine the Brittle – Ductile Transition (BDT) by using the information on the geothermal gradient, crustal composition (wet quartzite for the upper crust and granulite for the lower crust) and strain-rate constrained by geophysical observations. Crustal rheological properties also act as meaningful indicators in geothermal resource mapping. The geothermal resource database in a GIS environment has been presented for Saudi Arabia by Aboud et al. (2021). The spatial datasets involve the Curie depth (km), Temperature gradient (°C/km), Heat flow (mW/m^2), Fault density, Volcanic field density, and Seismic event density and are useful for identifying areas for geothermal potential.

The Najd Fault System (NFS) is the most conspicuous fault in the whole region, displaying left-lateral shear, which crosses the NHR in the NW-SE direction. Other faults and fractures developed in the area maintain a sympathetic trend to NFS (Figure 13a). No less prosperous are the NE-trending set of secondary faults and fractures in the region which are transverse to NFS (Trippanera et al., 2019); their origin has been ascribed mainly to the Red Sea transforms. The mutually high-angle faults present in NHR provide effective passage for geothermal heat and fluid transmission from deeper to shallower depths. These fault zones usually act as conduits, barriers, or a combined conduit-barrier system for heat and fluid transmission. The heat transmission also depends on the architecture of the fault and rock materials present in the fault zone (Caine et al., 1996). It has been reported by studies elsewhere that the geometrical fracture pattern along a wellbore increases the connection between the borehole and the nearly vertical fracture network associated with a local fault, wherever present (Vidal et al., 2017). An important conclusion derived from their study was to establish a good characterization of zones of fractures in a targeted natural reservoir that may allow an optimal exploitation of geothermal resources. However, no deep geothermal drilling data are available for NHR, save for some shallow-depth geohydrologic boreholes. Al-Shaibani (2003) reported results based only on a handful of shallow-depth geohydrologic boreholes drilled into the Madinah basaltic terrain in NHR. The lithology encountered as well as the stratigraphy based on the drilling for the fractured vesicular basalts for nearly 60m depth is illustrated in Figure 13b. Here, the general groundwater flow is directed to N – NNE, in a direction coincident with the Ayn er Zerqa springs to the south of Al-Madinah city where the sub-basalt flow is through alluvium layers (Al-Shaibani, 2003). Such faults are likely amenable to fluid flow due to high transmissivity in the source material. A conceptual model (Figure 13c) of the fracture system in the Al Madinah basaltic field is prepared where the NFS is intersected by orthogonal normal faults. This fault system is amenable to fluid flow due to high transmissivity in the source material (Table 3 for pumping test data). Mode of heat transfer by local fault systems, streams or springs is generally by conduction (Vidal et al., 2017). A schematic sectional model of the major permeable fracture zone identified from borehole stratigraphy in NHR where fractures in vesicular basalt, in particular within the thick pile of Madinah basalt, are speculated (Figure 13d). These fractures act as a medium of fluid flow and heat transmission. Geothermal drill data are therefore essential to improve our understanding of the transmission of heat by conduction to the surficial crust.

VI. CONCLUSIONS

We examined the potential geothermal prospect of NHR by investigating; (i) crustal rheological parameters derived from REF results, (ii) subsurface configuration of the low resistive zone detected by MT surveys, and (iii) seismic data on the depth horizons for the upper and lower crust based on REF seismic stations by constructing 2.5 km depth slices, (iv) present and analyze the elastic constants computed for the upper and lower crustal columns namely; Vp, Vp/Vs, ρ, σ and AI etc. and (v) gravity and rheological anomalies.

The main results derived from the study in NHR are:

(i) The values for Vp/Vs, ρ, σ and AI are significantly lower below NHR with respect to the surrounding crust due to high heat flow.
(ii) The GLZ over NHR bears a close relationship with the eastern vent axis extending regionally in the NNW-SSE direction and magma chamber.
(iii) Depth slices of rheological parameters along a traverse taken across the zone of GLZ unravels LVZ, LDZ, a Low Poisson Ratio (σ) and Young's Modulus (E) zones at crustal depths of 5 to 17.5 depth beneath the western vent axis which increases to 25 km depth toward the eastern vent axis. This result may be taken to imply a deeper root for the eastern vent axis as compared to the western vent axis.
(iv) It is beyond the purview of the present study to explain the origin of the rarefied crust in the region of the vent axes under northern Harrat Rahat. We can only speculate that it probably owes its origin to partial melting in the crust, related to the Afar plume.
(v) A conceptual geologic model is proposed for heat transfer in the geothermal system of NHR, in particular reference to the vesicular basalt unit in the Al Madinah volcanic field. Orthogonal fractures/faults crossing NHR are envisaged to play a significant role in heat transfer.

ACKNOWLEDGEMENT

Three of us (M.M., S.M. and E.I.) extend our appreciation to the Research Supporting Project number RSP 2023/R325, King Saud University, Riyadh, Saudi Arabia.

Statements & Declarations

Funding

The authors declare that no funds, grants, or other support were received during the preparation of this manuscript.

Competing Interests

The authors have no relevant financial or non-financial interests to disclose.

Author Contributions

All authors contributed to the study conception and design. Material preparation, data collection and analysis were performed by Manoj Mukhopadhyay and Basab Mukhopadhyay. The first draft of the manuscript was written by Manoj Mukhopadhyay and Basab Mukhopadhyay, and all authors commented on previous versions of the manuscript. All authors read and approved the final manuscript.

Data availability

Data used in the analysis of the rheological properties across NHR are already added in Tables 1 to 3 and included in the manuscript.

REFERENCES

1. Al-Amri, A., Abdelrahman, K., Mellors, R., & Harris, D. (2020). Geothermal potential of Harrat Rahat, Northern Arabian Shield: Geological constraints. *Lawrence Livermore National Laboratory, U.S.A., LLNL-JRNL-815125*, 1- 21.
2. Aboud, E., Qaddah, A., Harbi, H., & Alqahtani, F. (2021) Geothermal Resources Database in Saudi Arabia (GRDiSA): GIS model and geothermal favorability map. *Arabian J. Geosci., 14*, 112. https://doi.org/10.1007/s12517-020-06426-z.
3. Aboud, E., Alqahtani, F., Elmasry, N., Abdulfarraj, M., & Osman, H. (2022). Geothermal anomaly detection using potential field geophysical data in Raahat volcanic field, Madinah, Saudi Arabia. *J. Geol. Geophys., 11(4)*, 1026.
4. Aboud, E., Arafa-Hamed, T., Alqahtani, F., Marzouk, H., Elbarbary, S., Abdulfaraj, M., & Elmasry, N. (2023) The geothermal magmatic system at the northern Rahat volcanic field, Saudi Arabia, revealed from 3D magneto telluric inversion. *J. Volcano. Geotherm. Res., 437*, 107794.
5. Al-Dayel, M. (1988). Geothermal resources in Saudi Arabia. *Geothermics 17(2)*, 465–476. https://doi.org/10.1016/0375-6505(88)90076-4.
6. Al-Shaibani, A.M. (2003). Lava fields as potential groundwater sources in Western Saudi Arabia. In Sherif, Singh, & Al-Rashed (Eds.), *Hydrology & Water Resources*. Swets & Zeitinger, Lisse, ISBN 90 5809 548 7.
7. Anderson, D.L. (1989) *Theory of the Earth*. Blackwell Scientific Publications, Boston, USA. http://resolver.caltech.edu/CaltechBOOK:1989.001.
8. Bohannon, R.G., Naeser, C.W., Schmidt, D.L., & Zimmermann, R.A. (1989) The timing of uplift, volcanism, and rifting peripheral to the Red Sea: A case for passive rifting? *Journal of Geophysical Research, 94*, 1683–1701. https://doi.org/10.1029/JB094iB02p01683.
9. Brocher, T.M. (2005). Empirical relations between elastic wave speeds and density in the earth's crust. *Bull. Seism. Soc. Am., 95*, 2081-2092.
10. Brown, G.F. (1980). Physiographic Provinces of the Arabian Peninsula, *U. S. Geological Survey Prof. Paper 560-A, Plate 3, Scale 1: 4 000 000*. Min. Pet. Min. Resources, Kingdom of Saudi Arabia.
11. Caine, J. S., Evans, J. P., & Forster, C. B., (1996). Fault zone architecture and permeability structure. *Geology, 24(11)*, 1025–1028, https://doi.org/10.1130/0091-7613(1996)024<1025:FZAAPS>2.3.CO;2.
12. Camp, V.E., Hooper, P.R., Roobol, M.J., & White, D.L., (1987). The Madinah eruption, Saudi Arabia: magma mixing and simultaneous extrusion of three basaltic chemical types. *Bull. Volcanology 49*, 489–508.
13. Camp, V.E., & Roobol, M.J., (1989). The Arabian continental alkali basalt province: Part I. Evolution of Harrat Rahat, Kingdom of Saudi Arabia. *Geo. Soc. Am. Bull. 101*, 71–95.
14. Camp, V.E., & Roobol, M.J., (1991). Geologic map of the Cenozoic lava field of Harrat Rahat, Kingdom of Saudi Arabia: Ministry of Petroleum and Mineral Resources, Directorate General of Mineral Resources, 1 map sheet, 37 p.
15. Camp, V.E., & Roobol, M.J., (1992). Upwelling asthenosphere beneath Western Saudi Arabia and its regional implications. *J. Geophys. Res. 97*, 15255-15271.
16. Casertano, L., & Del Castillo, A. O., (1980) Vp/Vs ratio and its changes in the Travale geothermal field. In: S. Strub et al., (Eds.), *Advances in European Geothermal Research* © ECSC, EEC, EAEC, Brussels and Luxembourg.

17. Christensen, N.I., (1996) Poisson's ratio and crustal seismology. *J. Geophys. Res., 101*, 3139-3156.
18. Christensen, N. I., & Mooney, W. D., (1995) Seismic velocity structure and composition of the continental crust: A global view. *J. Geophys. Res., 100*, 9761 – 9788.
19. Civilini, F., Mooney, W.D., Savage, M.K., Townend, J., & Zahran, H., (2019). Crustal imaging of northern Harrat Rahat, Saudi Arabia, from ambient noise tomography. *Geophys. J. Int., 219*, 1532–1549. https://doi.org/10.1093/gji/ggz380
20. Coleman, R.G., Gregory, R.T., & Brown, G.F., (1983). Cenozoic volcanic rocks of Saudi Arabia. *U.S. Geological Survey Open-File Report OF-03-83*, 1-82.
21. Chang, S.J., Merino, M., Van der Lee, S., Stein, S., & Stein, C.A. (2011). Mantle flow beneath Arabia offset from the opening Red Sea. *Geophys. Res. Lett. 38*, L04301. https://doi.org/10.1029/2010gl045852.
22. Demange, J., (1984). Drilling for geothermal resources in Harrat Khayber region. *Technical report, Deputy Ministry for mineral resources, Ministry of Petroleum and Mineral Resources*, Riyadh.
23. Diaferia, G., & Cammarano, F., (2017). Seismic signature of the continental crust: What thermodynamics says. An example from the Italian Peninsula. *Tectonics 36*, 3192-3208. https://doi.org/10.1002/2016TC004405.
24. Downs, D.T., Stelten, M. E., Champion, D. E., Dietterich, H. R., Nawab, Z., Zahran, H., Hassan, K. & Shawali, J., (2018). Volcanic history of the northernmost part of the Harrat Rahat volcanic field, Saudi Arabia. *Geosphere, 14*, 1253–1282. https://doi.org/10.1130/GES01625.1
25. Downs, D.T., Robinson, J.E., Stelten, M.E., Champion, D.E., Dietterich, H.R., Sisson, T.W., Zahran, H., Hassan, K. & Shawali, J., (2019). Geologic Map of the Northern Harrat Rahat Volcanic Field, Kingdom of Saudi Arabia. *Scientific Investigations Map 3428, as Saudi Geological Survey Special Report SGS–SP–2019–2*, https://doi.org/10.3133/sim3428
26. Gercek, H., (2007). Poisson's ratio values for rocks. *Int. J. Rock Mechanics & Mining Sci.*, 44, 1-13.
27. Gettings, M. E., Blank Jr., H. R., Mooney, W.D. & Healey, J.H., (1986). Crustal structure of southwestern Saudi Arabia. *J. Geophys. Res. 91*, 6491-6512.
28. Head, M., Hickey, J., Gottsmann, J., & Fournier, N. (2021). Exploring the impact of thermally controlled crustal viscosity on volcanic ground deformation. Journal of Geophysical Research: Solid Earth, 126, e2020JB020724. https://doi.org/10.1029/2020JB020724
29. Heise, W., Bibby, H.M., Caldwell, T.G., Bannister, S.C., Ogawa, Y., Takakura, S., & Uchida, T., (2007). Melt distribution beneath a young continental rift: the Taupo Volcanic Zone, New Zealand. *Geophys. Res. Letters, 34(14),* L14313. https://doi.org/10.1029/2007GL029629
30. IGA Service GmbH, 2014. Best Practices Guide for Geothermal Exploration. C. Harvey, C. (Eds.), *GmbH, Bochum Univ., Germany*, 1- 196.
31. Italconsultant, (1979). Detailed investigation of the Medinah Region. *Final report, Thematic report no. 7*, Saudi Arabian Ministry of Agriculture and Water, Riyadh.
32. Jakobsson, S.P., Jonasson, K. & Sigurdsson, I.A., (2008). The three igneous rock series of Iceland. *JOKULL, 58,* 117-138.
33. Ji, S., Sun, S., Wang, Q., & Marcotte, D., (2010). Lame' parameters of common rocks in the Earth's crust and upper mantle. *J. Geophys. Res. 115*, B06314. https://dx.doi.org/10.1029/2009JB007134.
34. Kasahara, J., Hasada, Y., & Kuzume, H., (2020). Possibility of high Vp/Vs zone in the geothermal field suggested by the P-to-S conversion. *Proc. 45th Workshop Geoth. Reservoir Eng., Stanford Univ., California, Feb. 10-12, 2020*, SGP-TR-216 1.
35. Kaviani, A., Paul, A., Moradi, A., et al., (2020). Crustal and uppermost mantle shear wave velocity structure beneath the Middle East from surface wave tomography. *Geophys. J. Int. 221*, 1349–1365.
36. Kusznir, N. J., Vita-Finzi, C., Whitmarsh, R.B., England, P., Bott, M.H.P., Govers, R., Cartwright, J. & Murrell, S., (1991). The distribution of stress with depth in the lithosphere: thermos-rheological and geodynamic constraints. *Phil. Trans.: Physical Sci. Eng., 337 (1645), Tectonic Stress in the Lithosphere*, 95-110. URL:https://www.jstor.org.stable/53683

37. Kereszturi, G., Nemeth, K., Moufti, M. R. H., Cappello, A., Murcia, H., Ganci, G., Negro, C. D., Procter, J., & Zahran, H. M. A., (2016). Emplacement conditions of the 1256 AD Al-Madinah lava flow field in Harrat Rahat, Kingdom of Saudi Arabia - Insights from surface morphology and lava flow simulations. *J. Volcano. Geothermal Res. 309*, 14-30.
38. Langenheim, V.E., (2018). Gravity and physical property data of the northern Harrat Rahat, Saudi Arabia. *In: U.S. Geological Survey Data Release*, https://doi.org/10.5066/P9THCSE8.
39. Langenheim, V.E., Ritzinger, B.T., Zahran, H., Shareef, A., & Al-dahri, M., (2019). Crustal structure of the northern Harrat Rahat volcanic field (Saudi Arabia) from gravity and aeromagnetic data. *Tectonophys., 750*, 9-21.
40. Lim, J-A., Chang, S-J., Mai, P.M., & Zahran, H., (2020). Asthenospheric flow of plume material beneath Arabia inferred from S wave travel time tomography. *Journal of Geophysical Research Solid Earth 125*, e2020JB019668. https://doi.org/10.1029/2020JB019668.
41. Lees, J. M. & Wu, H. (2000) Poisson's ratio and porosity at Coso geothermal area, California. Journal of Volcanology and Geothermal Research 95, 157–173.
42. Lin, G., (2020). Spatio temporal variations of in situ Vp/Vs ratio within the Salton Sea Geothermal Field, southern California. *Geothermics, 84*, 101740. https://doi.org/10.1016/j.geothermics.2019.101740.
43. Mogren, S., Mukhopadhyay, B., Mukhopadhyay, M., Nandi, B.K., & Ibrahim, E. (2021). Spatial distribution of the rheological heterogeneities at crustal depths underneath the Harrat Rahat, western Saudi Arabia and their correspondence to Bouguer anomalies. *Journal of Volcanology and Geothermal Research 419*, 107387.
44. Muluneh, A. A., Keir, D. & Corti, G., (2021). Thermo-rheological properties of the Ethiopian lithosphere and evidence for transient fluid induced lower crustal seismicity beneath the Ethiopian rift. *Front. Earth Sci., 9*, 610165. https://doi.org/10.3389/feart.2021.610165
45. Musacchio, G., Mooney, W.D., Luetgert, J. H., & Christensen, N. I. (1997). Composition of the crust in the Grenville and Appalachian Provinces of North America inferred from VP/Vs ratios. *J. Geophys. Res. 102*, 15225-15241.
46. Murcia, H., Lindsay, J.M., Németh, K., Smith, I.E.M., Cronin, S.J., Moufti, M.R.H., El-Masry, N.N., & Niedermann, S., (2016). Geology and geochemistry of Late Quaternary volcanismin northern Harrat Rahat, Kingdom of Saudi Arabia: Implications for eruption dynamics, regional stratigraphy and magma evolution. In: Németh, K., Carrasco-Núñez, G., ArandaGómez, J.J., Smith, I.E.M. (Eds.), Monogenetic Volcanism. *Geo. Soc. London Spl. Publn. 446*, 173–204. https:// doi .org /10 .1144 /SP446.2.
47. Mukhopadhyay, M., Mukhopadhyay, B., Mogren, S., Nandi, B.K., & Ibrahim, E., (2022). Regional significance of crustal and sub-crustal rheological heterogeneities beneath the Harrat Lunayyir and their continuity into the neighboring harrats, Western Saudi Arabia – Perspectives of the Afar plume activity. *Journal of African Earth Sciences 186*, 104432.
48. Runge, M.G., Bebbington, M.S., Cronin, S.J., Lindsay, J.M., Kenedi, C.L., & Moufti, M.R.H., (2014). Vents to events: Determining an eruption event record from volcanic vent structures for the Harrat Rahat, Saudi Arabia. *Bulletin of Volcanology 76*. https:// doi .org /10 .1007/s00445 -014-0804-z.
49. Runge, M.G., Bebbington, M.S., Cronin, S.J., & Moufti, M.R., (2015). Sensitivity to volcanic boundary. *J. App. Volcanology 4*, 22. https://doi.org/10.1186/s13617.015-0040-z.
50. Rudnick, R. L., & Gao, S., (2014). Composition of the continental crust. In: Holland, H. D., Turekian, K. K. (Eds) *Treatise on Geochemistry, The Crust 3, 1st edition*, Elsevier-Pergamon, 1-64.
51. Schmidt, D.L., & Hadley, D.G., (1985). Stratigraphy of the Miocene Baid formation, southern Red Sea coastal plain, Kingdom of Saudi Arabia. *U. S. Geological Survey OFR 85-241*.
52. Stern, R.J., & Johnson, P., (2010). Continental lithosphere of the Arabian Plate: A geologic, petrologic, and geophysical synthesis. *Earth Sci. Reviews. 101*, 26-67.

53. Stern, R. J., & Johnson, P.R., (2019). Constraining the opening of the Red Sea: Evidence from the Neoproterozoic margins and Cenozoic magmatism for a volcanic rifted margin. In: Rasul, N., Stewart, I. (Eds.), *Geological Setting, Palaeoenvironment and Archaeology of the Red Sea*. Springer, Cham. https://doi.org/10.1007/978-3-319-99408-6_19.
54. Tang, Z., Julia, J., Zahran, H. & Mai, P. M., (2016). The lithospheric shear-wave velocity structure of Saudi Arabia: Young volcanism in an old shield. *Tectonophys., 680*, 8-27. https://dx.doi.org/1.1016/j.tecto.2016.05.004
55. Tang, Z., Mai, P. M., Julià, J. & Zahran, H., (2019). Shear velocity structure beneath Saudi Arabia from the joint inversion of P and S wave receiver functions, and Rayleigh wave group velocity dispersion data. *J. Geophys. Res. Solid Earth 124*, 4767-4787. https://doi.org/10.1029/2018JB017131
56. Telford, W. M., Geldart, L. P., Sheriff, R. E., & Keys, D. A., (1976). *Applied Geophysics*, Cambridge Univ. Press, Cambridge, U.K.
57. Trippanera, D., Ruch, J., Passone, L. & Jonsson, S., (2019). Structural mapping of dike-induced faulting in Harrat Lunayyir (Saudi Arabia) by using high resolution drone imagery. *Frontiers in Earth Sci., 7*, 168. doi: 10.3389/feart.2019.00168.
58. Vidal, J., Genter, A. & Chopin, F., (2017). Permeable fracture zones in the hard rocks of the geothermal reservoir at Rittershoffen, France. *J. Geophys. Res. Solid Earth, 122*, 4864-4887. https://doi.org/10.1002/2017JB014331.

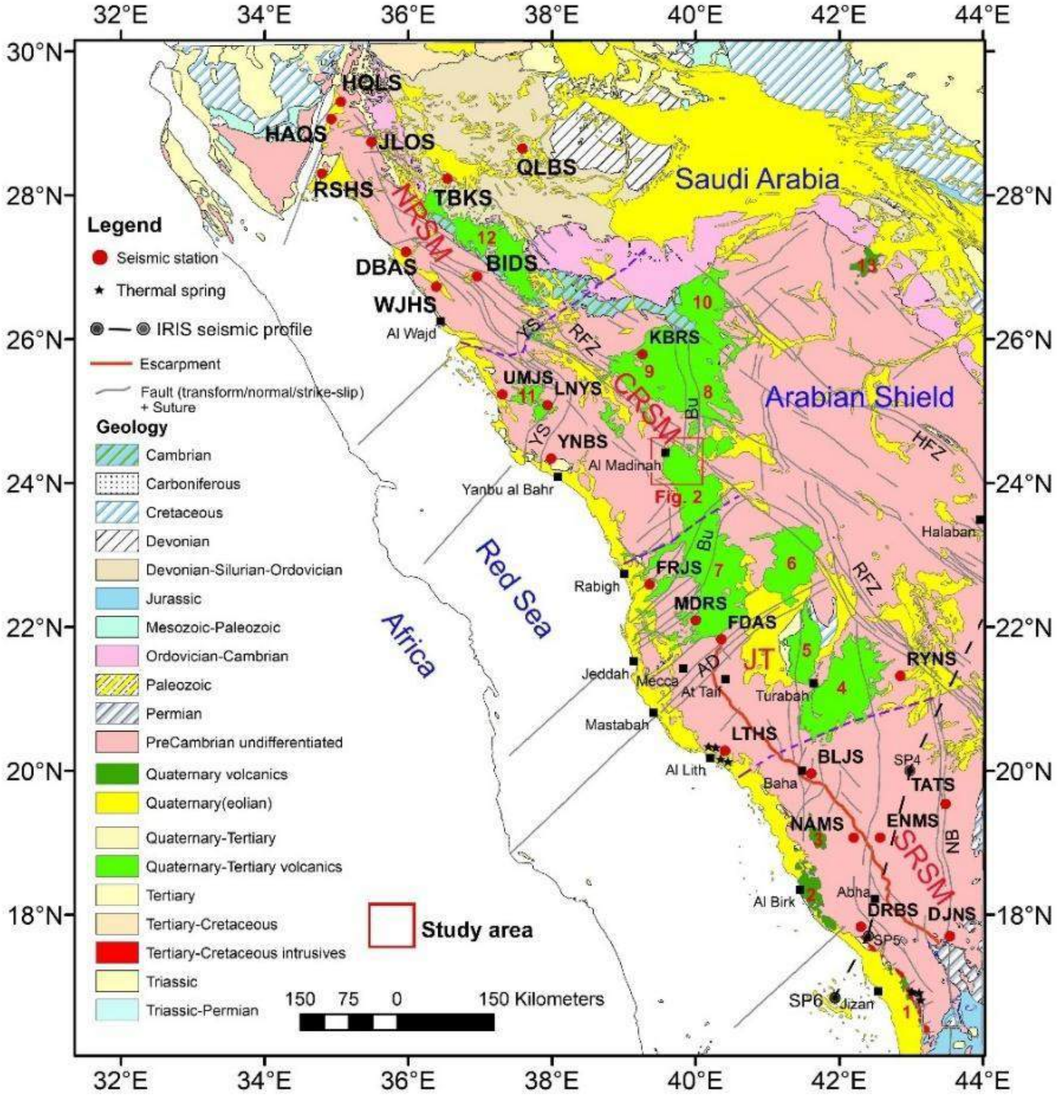

Figure 1: General geological map showing the Arabian Shield with Cenozoic volcanic fields in the Large Igneous Province of Saudi Arabia, adopted from Coleman et al. (1983) and USGS. The Arabian Shield along the Red Sea Margin (AS-RSM) are tectonically subdivided into three segments: North Red Sea Margin (NRSM), Central Red Sea Margin (CRSM) and Jeddah Terrane (JT), and Southern Red Sea Margin (SRSM). The Great Escarpment at the Arabian Shield margin in SW Saudi Arabia is after Schmidt and Hadley (1985). The location of seismic shot points done by USGS with numbers SP 5 to SP 4 (Gettings et al., 1986) is shown. The location of some broadband seismic stations in this terrain after Tang et al. (2016) is plotted. The detailed study area in the Northern Harrat Rahat within CRSM is boxed and its geological map in Figure 2. The harrats (in shades of green) in the Saudi Arabia LIP with their eruption age - 1: Tihama Asir (25-21 Ma), 2: Al Birk (4-0 Ma), 3: As Sirat (30 – 25 Ma), 4: Al Buqum (9-0Ma), 5: Hadan (28 – 25 Ma), 6: Al Kishb (2-0 Ma), 7: Rahat (10 – 0 Ma), 8: Khaybar (5-0 Ma), 9: Kura (11-5 Ma), 10: Ithnayn (3-0) Ma, 11: Lunayyir (1-0 Ma), 12: Uwayrid (9-0 Ma), and 13:Hutaymah (1.8 Ma). AD: Ad Damm Shear Zone, Bu: Bl'rUmq Suture Zone, HFZ: Halaban Fault Zone, RFZ: Rika Fault Zone, NB: Nibita Shear Zone, YS: Yanbu Shear Zone.

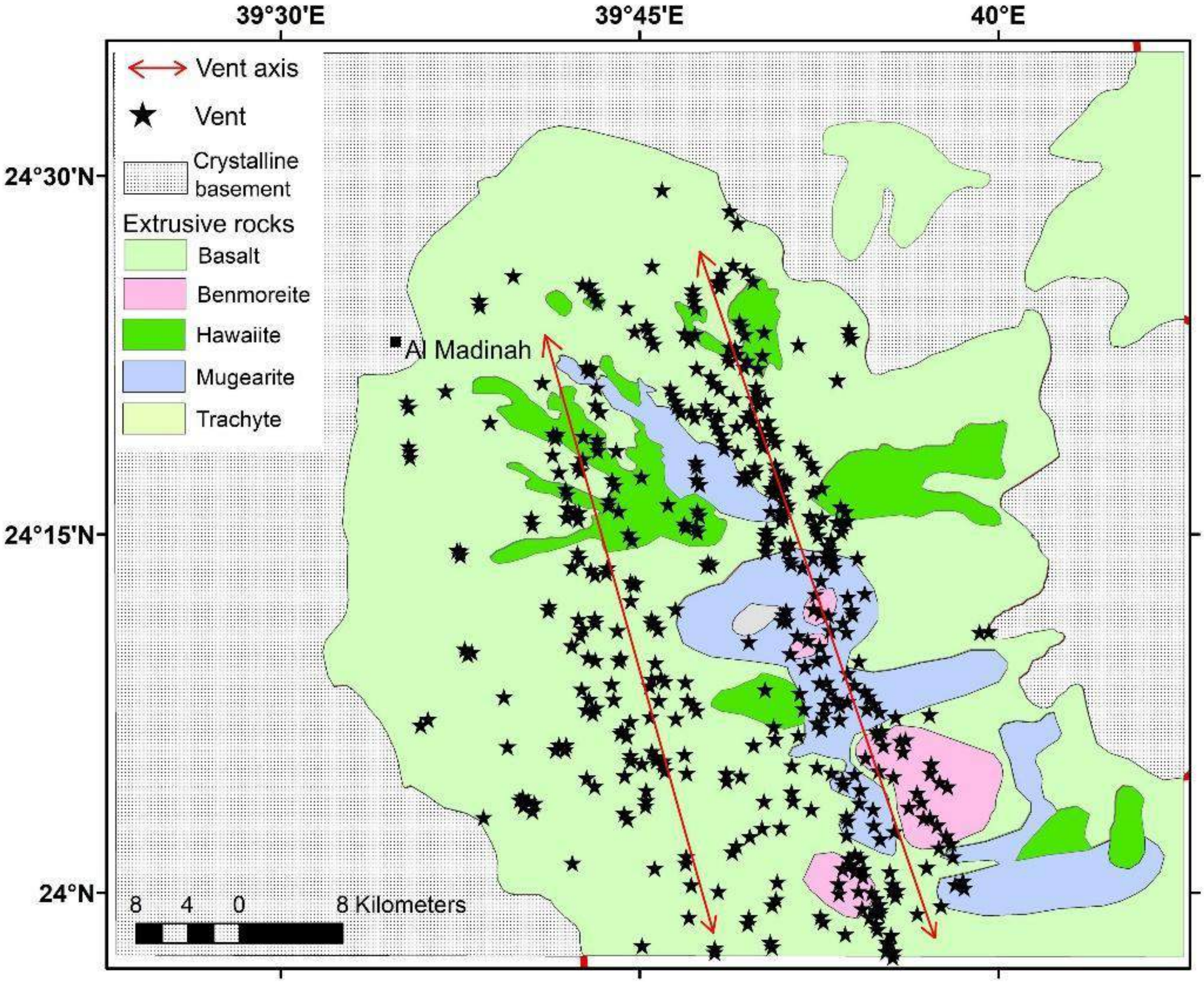

Figure 2: Geological map for Northern Harrat Rahat that forms the largest Cenozoic volcanic field hosted in Saudi Arabia (after Downs et al., 2019). Basalts and other eruptive rock types are shown by different colors and indexed. Red lines with arrows show locations and trends of vent axes across the Northern Harrat Rahat; they maintain a separation by ~10 km.

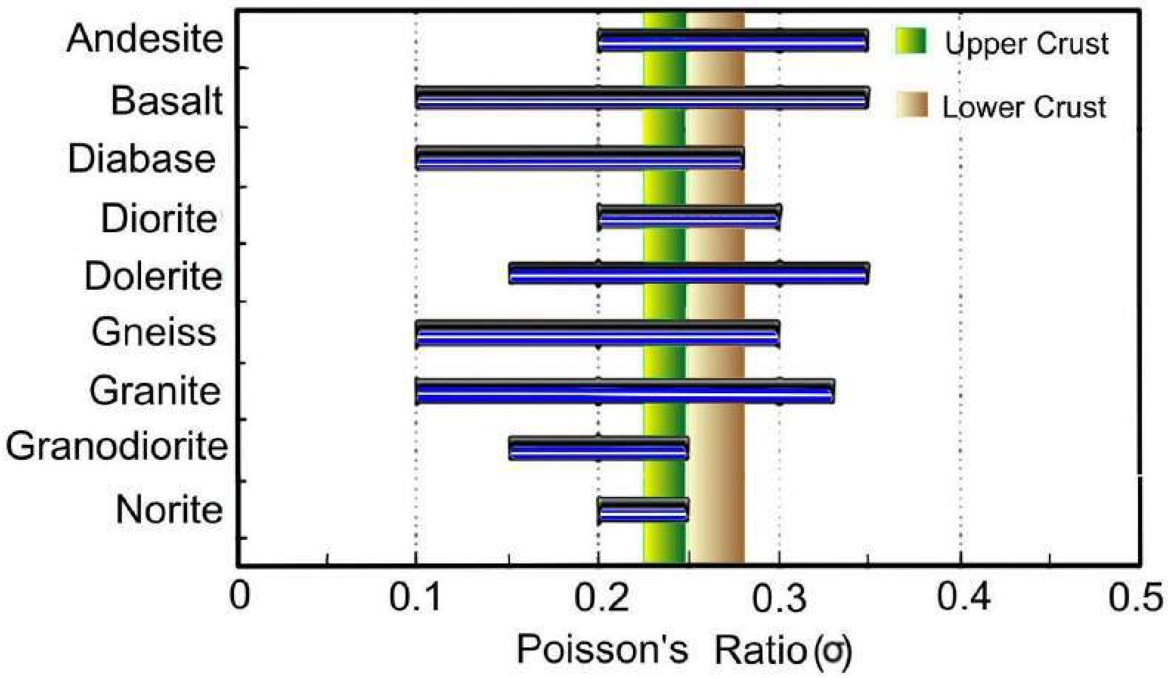

Figure 3: Typical range of values of Poisson's ratio (σ) for common rock types; redrawn after Gercek (2007). The σ values for the upper and lower crust obtained in the Northern Harrat Rahat are superposed on the bar diagram for identification of possible rock type. We infer granodiorite to diorite in the upper crust and a gabbroic lower crust.

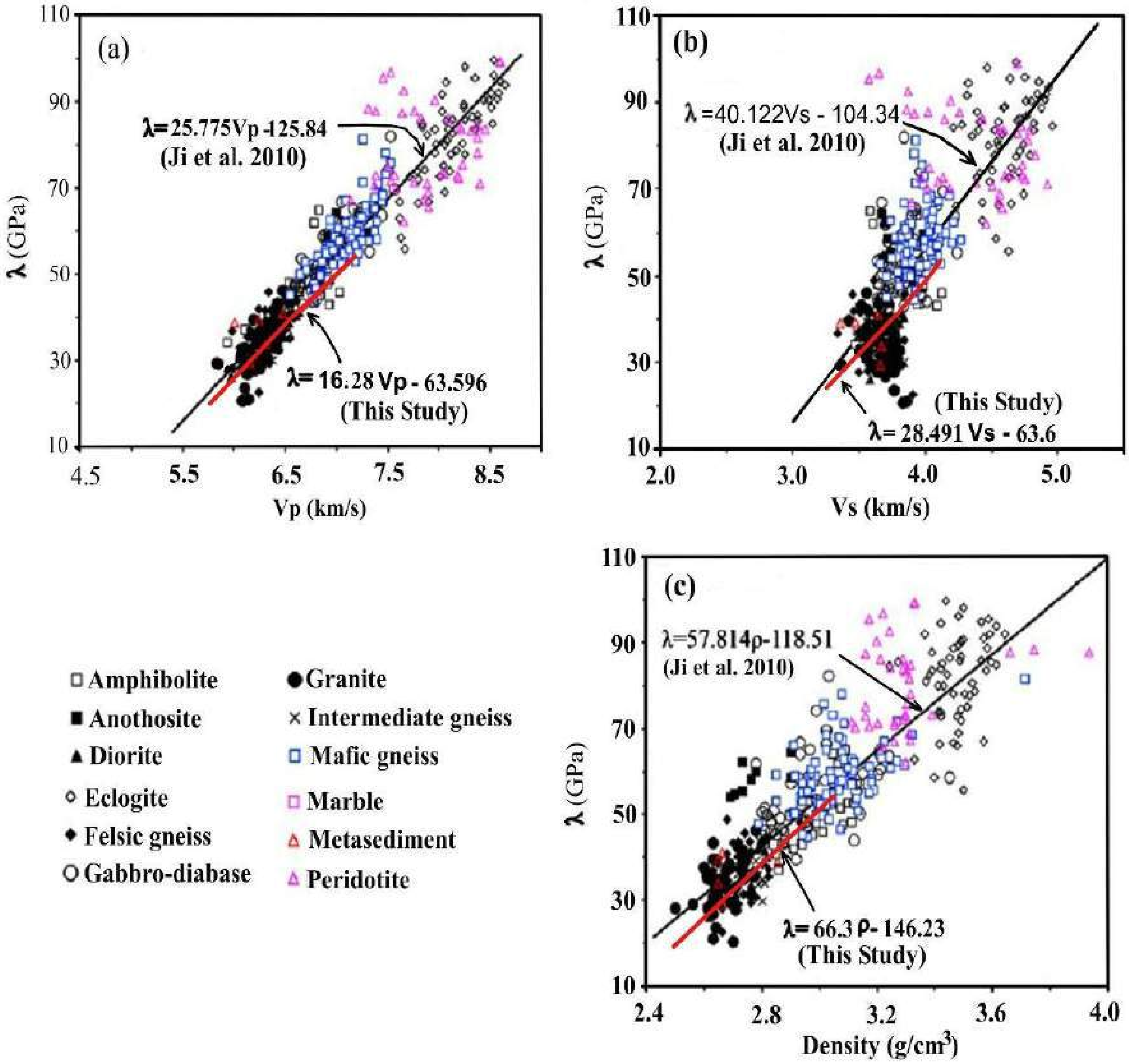

Figure 4: Relationships between Vp, Vs and ρ with λ for crustal rocks at a hydrostatic pressure of 600 MPa for 401 samples reported by Ji et al. (2010). The distribution of the regression relations [(a) Vp - λ, (b) Vs - λ, and (c) ρ - λ] obtained from the Northern Harrat Rahat and the regression and rock types inferred by Ji et al. (2010) are correlated to infer possible rock types below Northern Harrat Rahat. It shows felsic upper crust (with felsic and intermediate gneiss, and diorite) and a mafic lower crust (with mafic gneiss, subordinate amphibolite, gabbro, and diabase rocks).

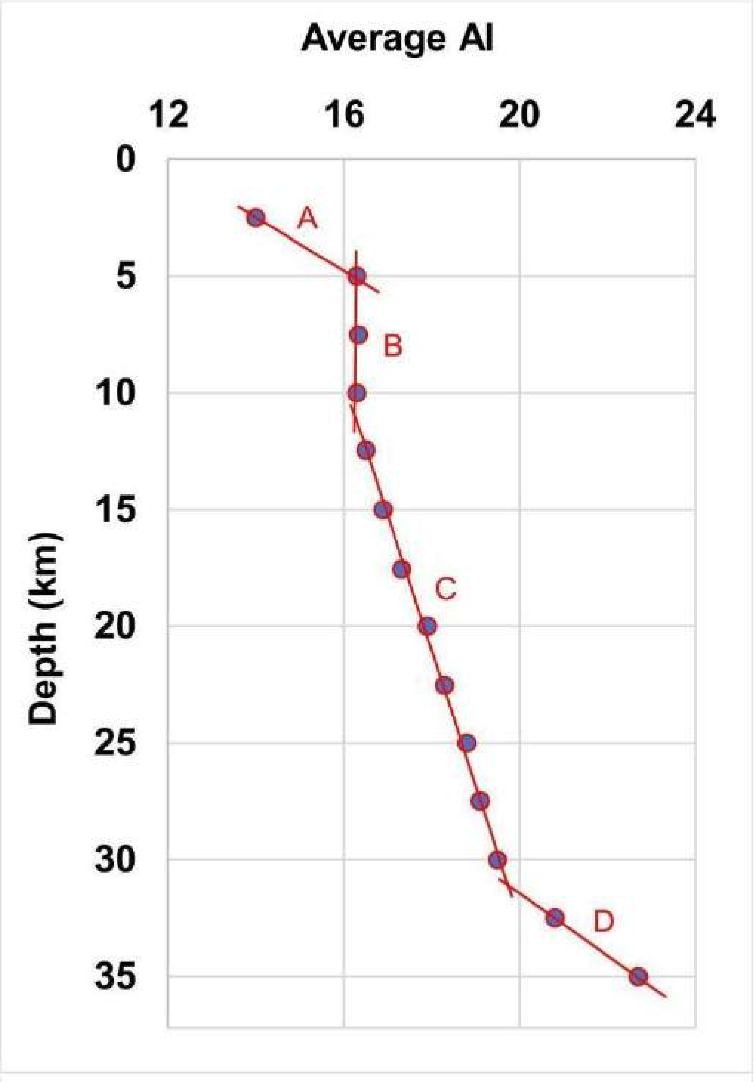

Figure 5: Depth wise plot of the average AI values in the NHR. From the change in slope of the curve, four zones (A to D) are identified. See text for explanation.

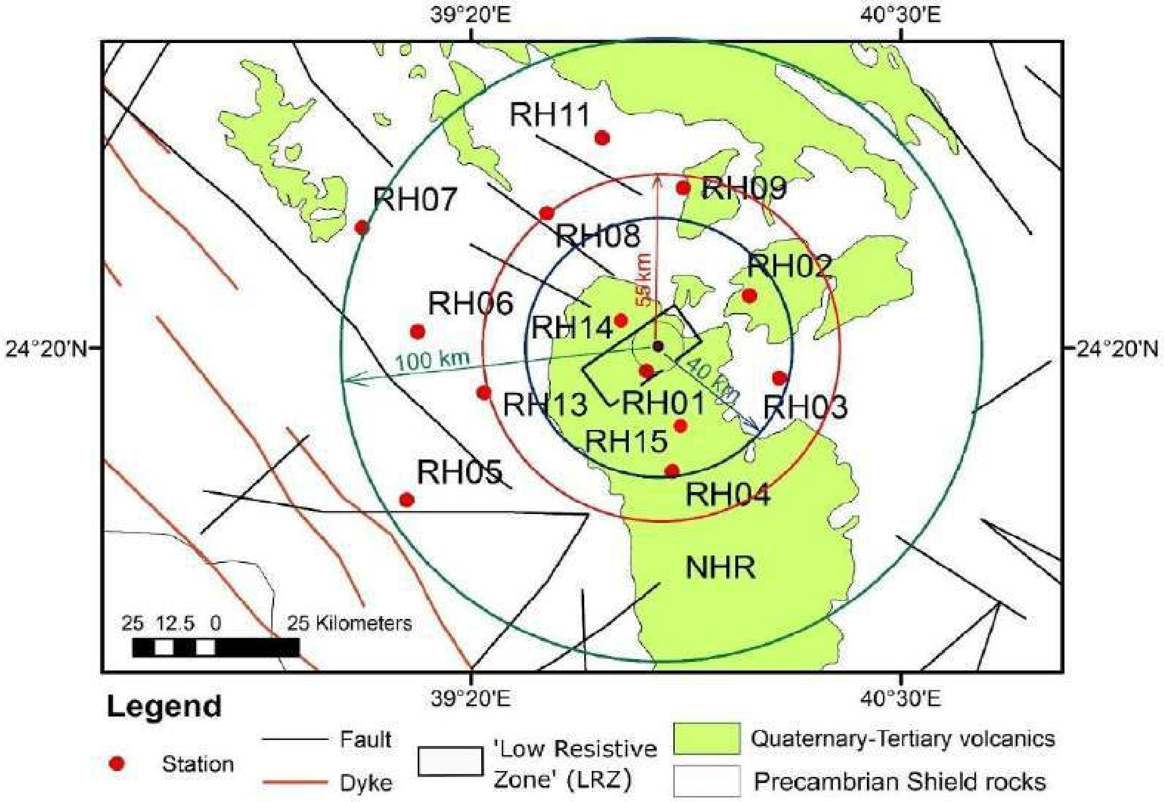

Figure 6: Four concentric circles are drawn circumventing the peak 'Low Resistive Zone' (LRZ) centered at 24°20'N, 39°50'E. Refer text for details. Seismic station RH01 is within a distance of 8 km from the peak LRZ.

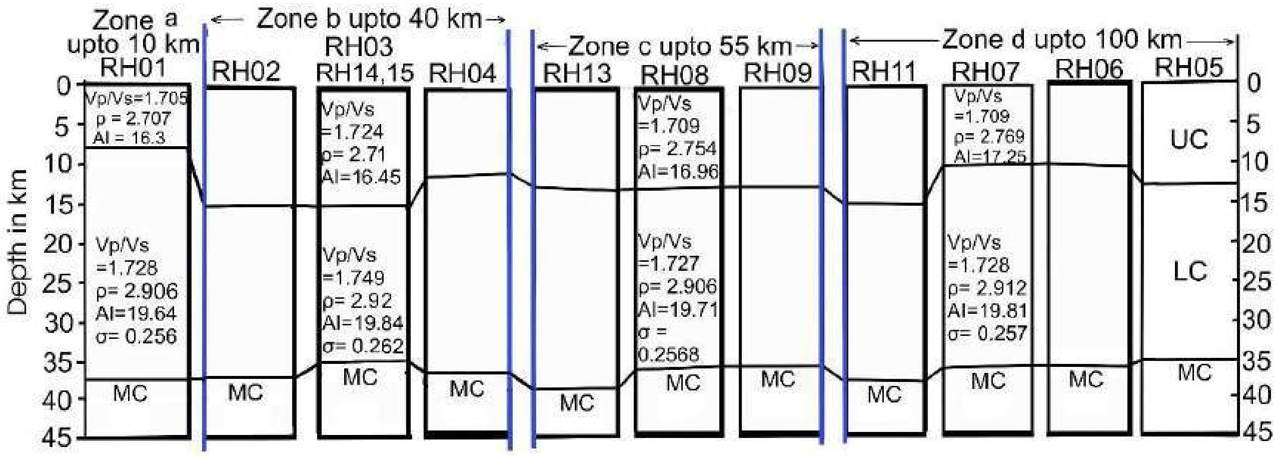

Figure 7: Location of REF seismic stations and the average distribution of rheological parameters within the upper and lower crustal columns within the radial zones a-d in figure 6 circumventing the LRZ discussed in the text. UC Upper crust, LC: Lower crust, MC: Moho.

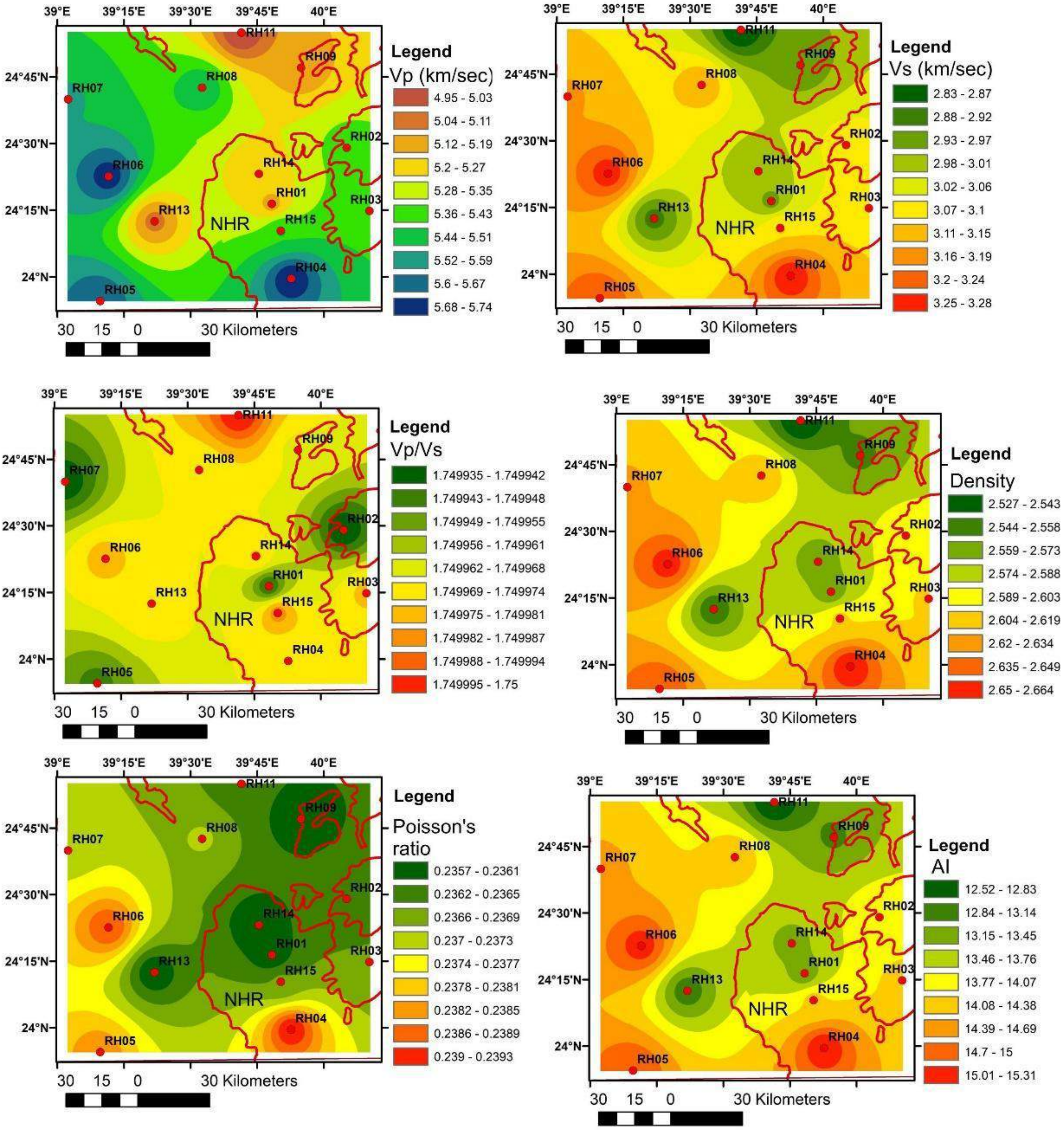

Figure 8: 2.5 km depth slices for selective crustal rheological parameters under the Northern Harrat Rahat (base data after Tang et al., 2019)

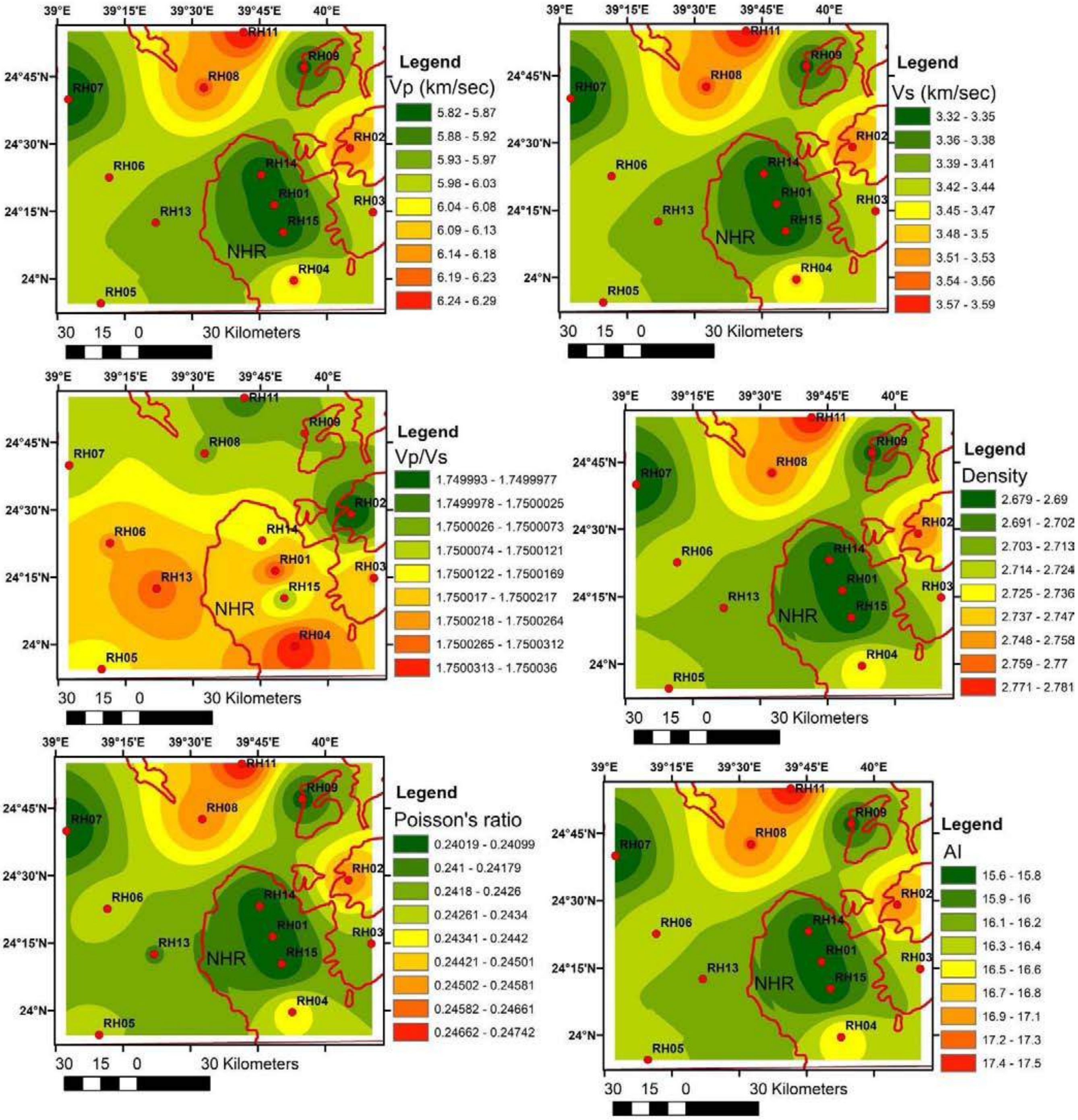

Figure 9: 5 km depth slices for selective crustal rheological parameters under the Northern Harrat Rahat (base data after Tang et al., 2019)

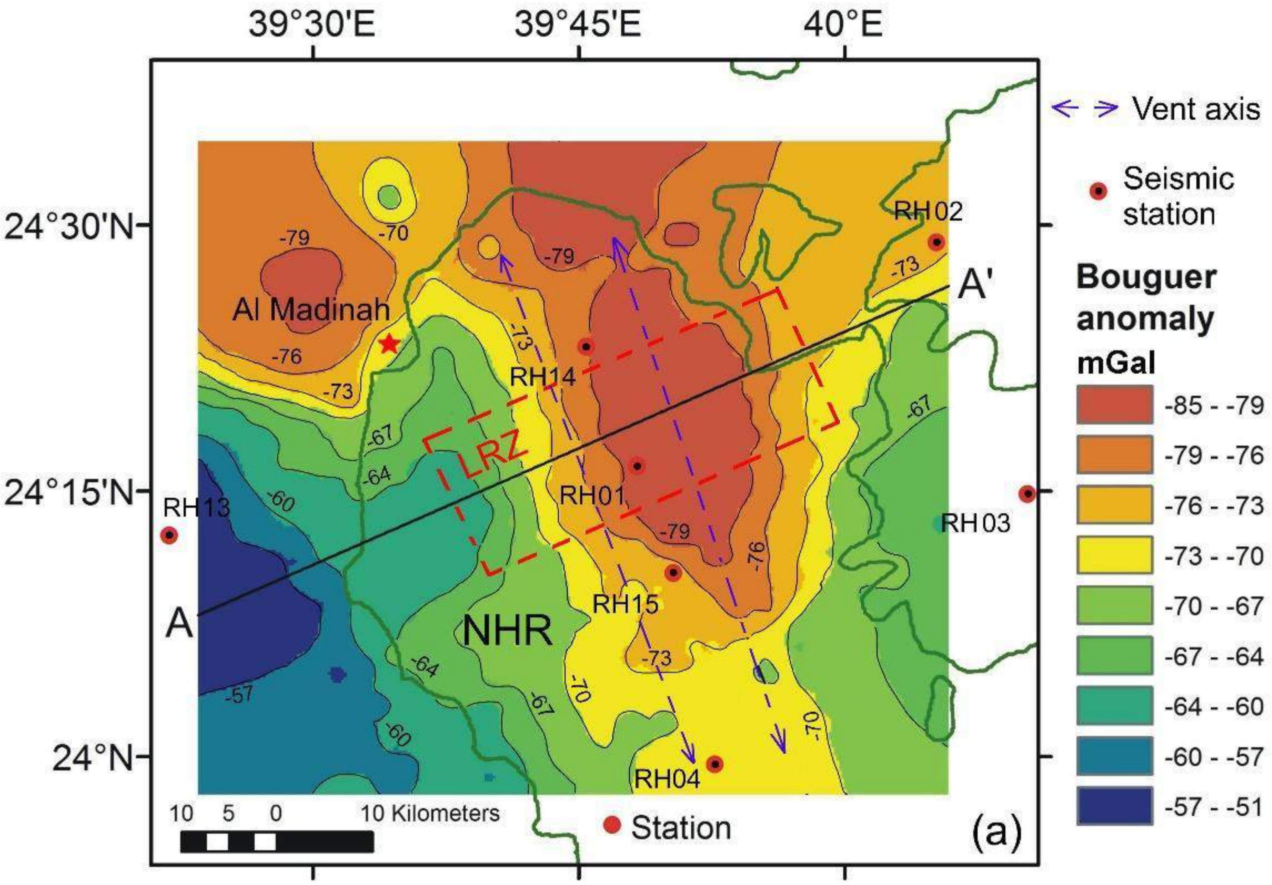

Figure 10: Bouguer anomaly map of Northern Harrat Rahat; redrawn after Langenheim (2018, 2019). The NNW-trending axial gravity low over NHR branches off westward to Al-Madinah. A-A' is a representative traverse illustrated on Figure 11. Red circles, REF seismic stations. Vent axes are also marked. Refer text for discussion.

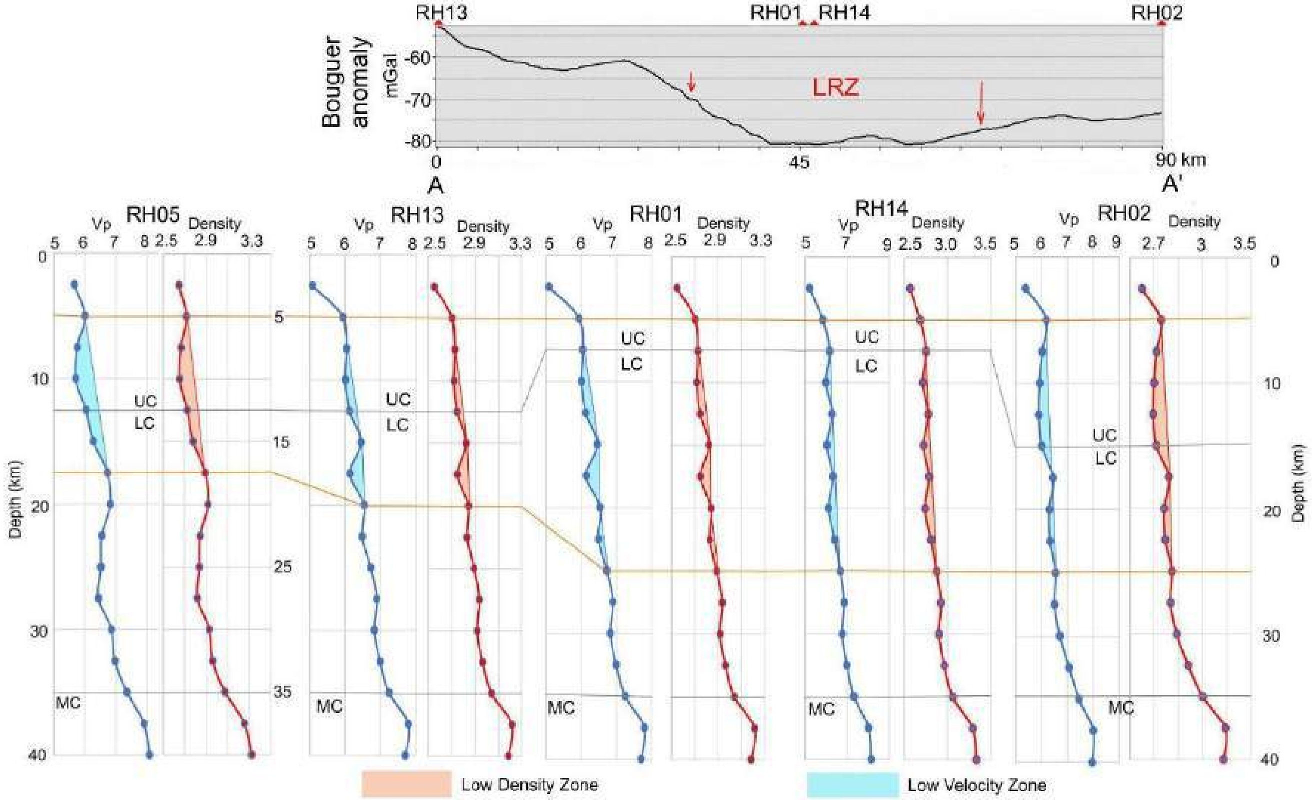

Figure 11: Plot for 2.5 km depth slices for Vp and Density underlying the five numbers of REF seismic stations, namely; RH05, RH13, RH01, RH14 and RH02 in bottom pannel. The gravity profile with gravity low zone (along the traverse A-A' of figure 10) and low resistivity zone (LRZ) are plotted in top pannel. The boundaries between upper crust (UC), lower crust (LC), and Moho (MC) are marked. Low velocity and low density zones are identified in depth section and marked.

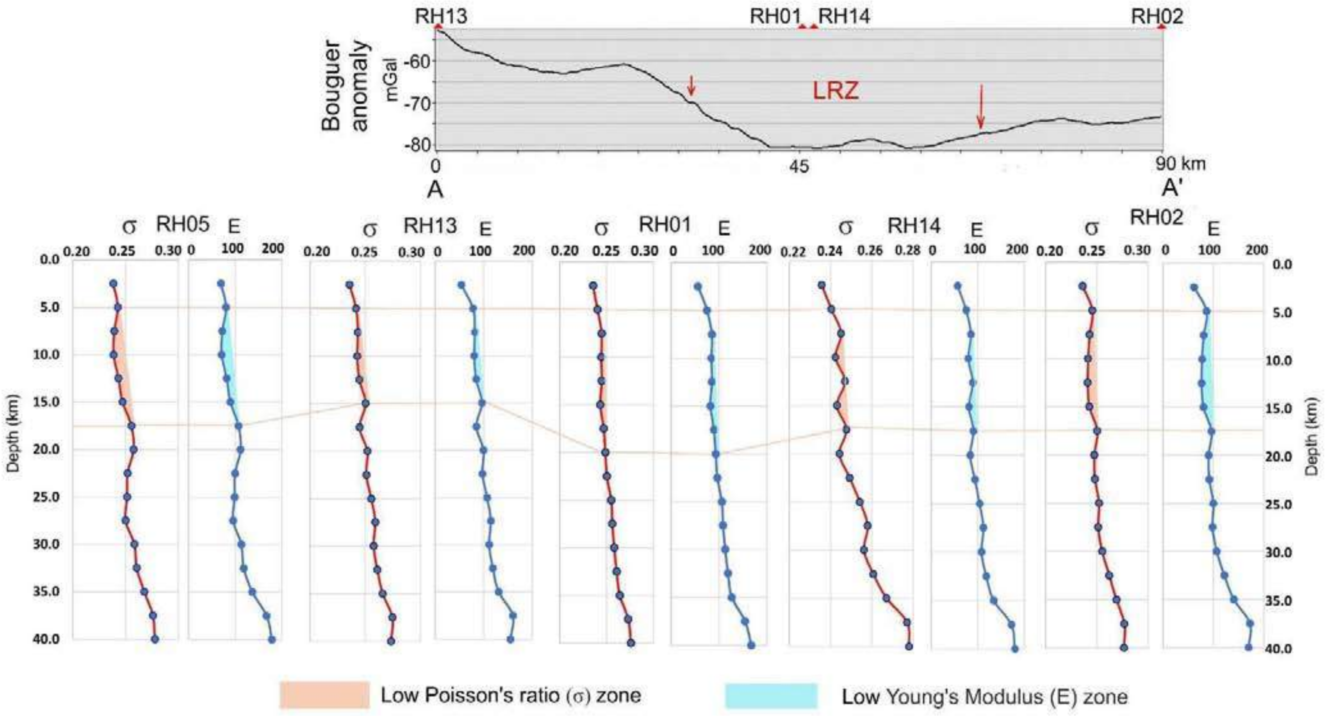

Figure 12: Plot for 2.5 km depth slices for and Poisson Ratio (σ) and Young's Modulus (E) underlying the five numbers of REF seismic stations, namely; RH05, RH13, RH01, RH14 and RH02 in bottom panel. The gravity profile with gravity low zone (along the traverse A-A' of figure 10) and low resistivity zone (LRZ) are plotted in the top panel. Low Poisson Ratio (σ) and low Young's Modulus (E) zones are identified in depth sections and marked.

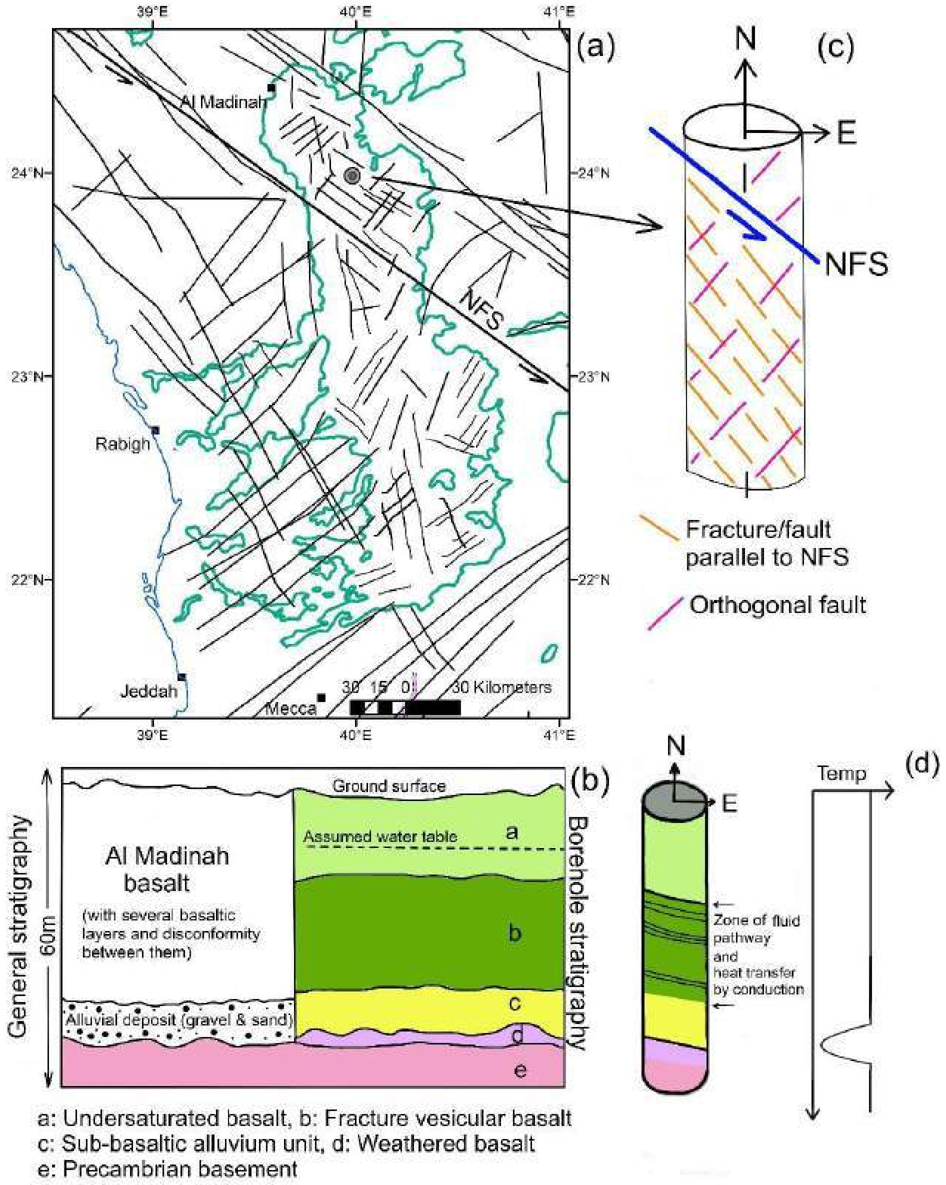

Figure 13: (a) Two dominant patterns of fractures and faulting across the Harrat Rahat and the Al-Madinah – Mecca region further north (adopted from: Coleman et al., 1983; Trippanera et al., 2019). One of them follows the left- lateral Najd Fault System (NFS) and its sympathetic parallel faults, while the other orthogonal normal faults are developed parallel to the Red Sea transforms. (b) Depicts the Borehole location, the general stratigraphy of the region from geological mapping and the borehole stratigraphy in NHR (after Al-Shaibani, 2003), (c) Conceptual model of fractures and faults in Madinah basalt in north part of NHR where the NFS is by far the most fault. The network of the fault system is supposedly amenable for fluid flow, and heat transfer to local streams or spring by conduction, (d) Schematic section of the major permeable fracture zone, including the fractured and vesicular basalt in the Medinah region, serve as fluid pathway, transmitting the heat by conduction and creating a probable temperature profile.

Table 1: The computed elastic constants up to 40 km depth for the 13 seismic broadband stations around Northern Harrat Rahat (REF data source: Tang et al., 2019). Abbreviations are: P-wave velocity, V_P; Shear-wave velocity, V_S; Density (g/cm^3), ρ; Lame's Second constant (Shear Modulus), μ; Lame's First constant, λ; Bulk Modulus, K; Young's Modulus, E; and Poisson Ratio, σ; Acoustic impedance, AI; Thickness of upper crust, h_{UC}; thickness of lower crust, h_{LC}.

Seismic Stations	Latitude	Longitude	Depth (Km)	Vp (km/s)	Vs (km/s)	Depth (Km)	Vp/Vs	Density (g/cm³)	Lame's First constant, (λ)	Shear Modulus (μ)	Bulk Modulus (K)	Young's Modulus (E)	Poisson's Ratio (σ)	Acoustic impedance (AI)
RH01	24.273	39.805	2.5	5.1569	2.9469	2.5	1.74994	2.5595	23.6116	22.2270	38.4295	55.9032	0.2357	13.1989
	24.273	39.805	5	5.8325	3.3328	5	1.75003	2.6817	31.6523	29.7874	51.5103	74.9206	0.2404	15.6412
	24.273	39.805	7.5	6.1372	3.5069	7.5	1.75004	2.7468	35.8961	33.7806	58.4163	84.9644	0.2449	16.8574
	24.273	39.805	10	6.1101	3.4914	10	1.75004	2.7407	35.5020	33.4089	57.7743	84.0296	0.2444	16.7460
	24.273	39.805	12.5	6.1426	3.5101	12.5	1.74998	2.7480	35.9708	33.8573	58.5421	85.1556	0.2450	16.8797
	24.273	39.805	15	6.0524	3.4586	15	1.74996	2.7280	34.6666	32.6320	56.4210	82.0733	0.2435	16.5109
	24.273	39.805	17.5	6.2644	3.5796	17.5	1.75003	2.7759	37.7957	35.5691	61.5082	89.4626	0.2470	17.3894
	24.273	39.805	20	6.3623	3.6356	20	1.75000	2.7991	39.3104	36.9980	63.9754	93.0555	0.2488	17.8090
	24.273	39.805	22.5	6.4509	3.6863	22.5	1.74997	2.8208	40.7225	38.3313	66.2764	96.4080	0.2504	18.1967
	24.273	39.805	25	6.6912	3.8236	25	1.74997	2.8825	44.7716	42.1416	72.8657	105.9916	0.2551	19.2872
	24.273	39.805	27.5	6.747	3.8555	27.5	1.74997	2.8974	45.7567	43.0698	74.4696	108.3258	0.2562	19.5489
	24.273	39.805	30	6.8538	3.9164	30	1.75003	2.9267	47.6992	44.8896	77.6253	112.9051	0.2583	20.0587
	24.273	39.805	32.5	6.9845	3.9911	32.5	1.75002	2.9636	50.1600	47.2065	81.6307	118.7323	0.2609	20.6991
	24.273	39.805	35	7.1542	4.0881	35	1.75001	3.0134	53.5099	50.3613	87.0838	126.6665	0.2642	21.5583
	24.273	39.805	37.5	7.6872	4.3927	37.5	1.74999	3.1829	65.2534	61.4162	106.1971	154.4706	0.2733	24.4674
	24.273	39.805	40	7.9109	4.5206	40	1.74997	3.2596	70.7680	66.6124	115.1758	167.5385	0.2762	25.7863
RH02	24.484	40.086	2.5	5.3884	3.0792	2.5	1.74994	2.5983	26.1694	24.6353	42.5928	61.9602	0.2363	14.0004
	24.484	40.086	5	6.1857	3.5347	5	1.74999	2.7577	36.6080	34.4554	59.5781	86.6604	0.2457	17.0585
	24.484	40.086	7.5	6.0225	3.4414	7.5	1.75001	2.7215	34.2475	32.2314	55.7348	81.0671	0.2430	16.3902
	24.484	40.086	10	5.9246	3.3854	10	1.75004	2.7007	32.8917	30.9524	53.5264	77.8511	0.2416	16.0005
	24.484	40.086	12.5	5.8932	3.3676	12.5	1.74997	2.6942	32.4601	30.5537	52.8291	76.8464	0.2412	15.8772
	24.484	40.086	15	6.009	3.4338	15	1.74996	2.7186	34.0534	32.0548	55.4230	80.6216	0.2428	16.3360
	24.484	40.086	17.5	6.4542	3.688	17.5	1.75005	2.8216	40.7837	38.3778	66.3686	96.5277	0.2505	18.2113
	24.484	40.086	20	6.2997	3.5998	20	1.75001	2.7842	38.3360	36.0793	62.3886	90.7452	0.2477	17.5396
	24.484	40.086	22.5	6.3328	3.6188	22.5	1.74997	2.7921	38.8459	36.5641	63.2217	91.9635	0.2483	17.6816
	24.484	40.086	25	6.5477	3.7416	25	1.74997	2.8451	42.3162	39.8306	68.8697	100.1790	0.2523	18.6290
	24.484	40.086	27.5	6.504	3.7166	27.5	1.74999	2.8341	41.5920	39.1472	67.6899	98.4606	0.2515	18.4327
	24.484	40.086	30	6.7058	3.8318	30	1.75004	2.8864	45.0341	42.3796	73.2869	106.5925	0.2554	19.3554
	24.484	40.086	32.5	7.054	4.0308	32.5	1.75002	2.9837	51.5116	48.4776	83.8297	121.9295	0.2623	21.0472
	24.484	40.086	35	7.4352	4.2486	35	1.75004	3.1003	59.4673	55.9627	96.7754	140.7564	0.2693	23.0515
	24.484	40.086	37.5	7.9956	4.569	37.5	1.74997	3.2894	72.9536	68.6697	118.7330	172.7128	0.2771	26.3011
	24.484	40.086	40	7.9525	4.5443	40	1.74999	3.2742	71.8390	67.6144	116.9148	170.0601	0.2766	26.0381
RH03	24.247	40.172	2.5	5.4265	3.1009	2.5	1.74998	2.6049	26.6113	25.0479	43.3097	62.9988	0.2365	14.1357

	24.247	40.172	5	5.9842	3.4195	5	1.75002	2.7133	33.7116	31.7263	54.8623	79.7970	0.2425	16.2368
	24.247	40.172	7.5	5.9442	3.3966	7.5	1.75004	2.7048	33.1601	31.2050	53.9632	78.4864	0.2419	16.0779
	24.247	40.172	10	5.9824	3.4185	10	1.75001	2.7129	33.6855	31.7032	54.8208	79.7387	0.2424	16.2296
	24.247	40.172	12.5	5.8823	3.3613	12.5	1.75001	2.6919	32.3157	30.4141	52.5916	76.4961	0.2410	15.8346
	24.247	40.172	15	6.121	3.4978	15	1.74996	2.7431	35.6537	33.5612	58.0276	84.4103	0.2446	16.7907
	24.247	40.172	17.5	6.5729	3.7559	17.5	1.75002	2.8516	42.7435	40.2265	69.5610	101.1765	0.2528	18.7431
	24.247	40.172	20	6.2949	3.597	20	1.75004	2.7831	38.2643	36.0085	62.2697	90.5680	0.2476	17.5191
	24.247	40.172	22.5	6.4532	3.6876	22.5	1.74997	2.8214	40.7603	38.3661	66.3375	96.4957	0.2505	18.2069
	24.247	40.172	25	6.556	3.7463	25	1.74999	2.8472	42.4570	39.9604	69.0970	100.5063	0.2525	18.6665
	24.247	40.172	27.5	6.5314	3.7322	27.5	1.75001	2.8410	42.0481	39.5729	68.4298	99.5323	0.2520	18.5556
	24.247	40.172	30	6.7326	3.8472	30	1.75000	2.8935	45.5038	42.8271	74.0550	107.7167	0.2559	19.4810
	24.247	40.172	32.5	6.9832	3.9903	32.5	1.75004	2.9632	50.1377	47.1816	81.5918	118.6707	0.2609	20.6927
	24.247	40.172	35	7.2938	4.1679	35	1.74999	3.0559	56.4017	53.0850	91.7913	133.5165	0.2668	22.2890
	24.247	40.172	37.5	7.9123	4.5213	37.5	1.75001	3.2601	70.8096	66.6431	115.2378	167.6177	0.2762	25.7947
	24.247	40.172	40	8.0132	4.579	40	1.74999	3.2957	73.4180	69.1018	119.4854	173.8009	0.2772	26.4091
	23.993	39.878	2.5	5.7448	3.2828	2.5	1.74997	2.6642	30.5031	28.7117	49.6440	72.2135	0.2393	15.3054
	23.993	39.878	5	6.0861	3.4777	5	1.75004	2.7354	35.1547	33.0829	57.2098	83.2095	0.2440	16.6479
	23.993	39.878	7.5	6.0445	3.4539	7.5	1.75005	2.7263	34.5613	32.5229	56.2430	81.8013	0.2434	16.4789
	23.993	39.878	10	5.8782	3.3589	10	1.75004	2.6911	32.2626	30.3611	52.5032	76.3637	0.2410	15.8186
	23.993	39.878	12.5	6.0922	3.4813	12.5	1.74998	2.7367	35.2382	33.1678	57.3498	83.4213	0.2441	16.6728
	23.993	39.878	15	6.0217	3.441	15	1.74999	2.7213	34.2340	32.2218	55.7150	81.0424	0.2430	16.3870
	23.993	39.878	17.5	6.3578	3.6329	17.5	1.75006	2.7981	39.2448	36.9287	63.8637	92.8833	0.2487	17.7895
	23.993	39.878	20	6.3504	3.6287	20	1.75005	2.7963	39.1274	36.8200	63.6739	92.6093	0.2486	17.7575
	23.993	39.878	22.5	6.6119	3.7783	22.5	1.74997	2.8616	43.4001	40.8516	70.6342	102.7468	0.2535	18.9209
	23.993	39.878	25	6.6496	3.7998	25	1.74999	2.8715	44.0493	41.4600	71.6890	104.2777	0.2543	19.0943
	23.993	39.878	27.5	6.6728	3.8131	27.5	1.74997	2.8776	44.4497	41.8396	72.3425	105.2317	0.2547	19.2017
	23.993	39.878	30	6.8157	3.8946	30	1.75004	2.9161	47.0020	44.2316	76.4894	111.2505	0.2576	19.8755
	23.993	39.878	32.5	7.0465	4.0265	32.5	1.75003	2.9815	51.3651	48.3387	83.5906	121.5804	0.2621	21.0094
	23.993	39.878	35	7.1083	4.0618	35	1.75004	2.9997	52.5893	49.4898	85.5821	124.4758	0.2633	21.3228
	23.993	39.878	37.5	7.741	4.4235	37.5	1.74997	3.2010	66.5444	62.6358	108.3011	157.5371	0.2740	24.7792
RHo 4	23.993	39.878	40	7.8368	4.4782	40	1.74999	3.2338	68.9029	64.8522	112.1372	163.1124	0.2753	25.3429
	23.909	39.161	2.5	5.6567	3.2325	2.5	1.74995	2.6472	29.3838	27.6602	47.8237	69.5685	0.2383	14.9741
	23.909	39.161	5	6.0022	3.4298	5	1.75001	2.7171	33.9623	31.9630	55.2708	80.3922	0.2427	16.3087
	23.909	39.161	7.5	5.7559	3.289	7.5	1.75005	2.6664	30.6512	28.8439	49.8803	72.5478	0.2394	15.3476
	23.909	39.161	10	5.7016	3.258	10	1.75003	2.6558	29.9549	28.1900	48.7480	70.9028	0.2388	15.1422
	23.909	39.161	12.5	6.0386	3.4507	12.5	1.74996	2.7250	34.4712	32.4473	56.1025	81.6090	0.2433	16.4551
	23.909	39.161	15	6.2725	3.5843	15	1.74999	2.7778	37.9165	35.6870	61.7076	89.7579	0.2472	17.4238
	23.909	39.161	17.5	6.7188	3.8392	17.5	1.75005	2.8898	45.2646	42.5946	73.6607	107.1338	0.2556	19.4162
RHo 5	23.909	39.161	20	6.8201	3.8972	20	1.75000	2.9173	47.0783	44.3090	76.6174	111.4439	0.2576	19.8965
	23.909	39.161	22.5	6.5348	3.7342	22.5	1.74999	2.8418	42.1022	39.6274	68.5202	99.6684	0.2520	18.5709
	23.909	39.161	25	6.5084	3.7191	25	1.74999	2.8352	41.6652	39.2152	67.8084	98.6319	0.2515	18.4524
	23.909	39.161	27.5	6.432	3.6754	27.5	1.75001	2.8161	40.4213	38.0419	65.7824	95.6816	0.2501	18.1134
	23.909	39.161	30	6.8573	3.9184	30	1.75003	2.9276	47.7638	44.9504	77.7304	113.0580	0.2584	20.0756

	23.909	39.161	32.5	6.9719	3.9839	32.5	1.75002	2.9600	49.9183	46.9790	81.2373	118.1600	0.2606	20.6366
	23.909	39.161	35	7.3565	4.2037	35	1.75001	3.0754	57.7438	54.3460	93.9741	136.6888	0.2679	22.6243
	23.909	39.161	37.5	7.9047	4.517	37.5	1.74999	3.2574	70.6135	66.4621	114.9211	167.1618	0.2761	25.7490
	23.909	39.161	40	8.0896	4.6227	40	1.74997	3.3231	75.4436	71.0120	122.7845	178.6045	0.2779	26.8824
	24.377	39.192	2.5	5.71	3.2629	2.5	1.74998	2.6574	30.0582	28.2922	48.9195	71.1586	0.2389	15.1738
	24.377	39.192	5	6.0248	3.4427	5	1.75002	2.7220	34.2804	32.2616	55.7879	81.1434	0.2431	16.3995
	24.377	39.192	7.5	5.7619	3.2924	7.5	1.75006	2.6676	30.7298	28.9164	50.0072	72.7306	0.2395	15.3704
	24.377	39.192	10	6.0221	3.4412	10	1.75000	2.7214	34.2408	32.2266	55.7249	81.0548	0.2430	16.3886
	24.377	39.192	12.5	6.1375	3.5072	12.5	1.74997	2.7468	35.8956	33.7872	58.4202	84.9793	0.2449	16.8587
	24.377	39.192	15	6.0477	3.4559	15	1.74996	2.7270	34.6003	32.5689	56.3126	81.9146	0.2434	16.4919
	24.377	39.192	17.5	6.4011	3.6577	17.5	1.75003	2.8086	39.9280	37.5751	64.9778	94.5080	0.2495	17.9779
	24.377	39.192	20	6.3103	3.6058	20	1.75004	2.7867	38.5021	36.2323	62.6567	91.1309	0.2479	17.5850
	24.377	39.192	22.5	6.5582	3.7476	22.5	1.74997	2.8478	42.4921	39.9960	69.1558	100.5952	0.2525	18.6765
	24.377	39.192	25	6.7434	3.8535	25	1.74994	2.8964	45.6901	43.0107	74.3635	108.1763	0.2561	19.5319
	24.377	39.192	27.5	6.727	3.844	27.5	1.75000	2.8920	45.4046	42.7337	73.8934	107.4817	0.2558	19.4547
	24.377	39.192	30	6.5642	3.7509	30	1.75003	2.8493	42.5983	40.0881	69.3235	100.8288	0.2526	18.7037
	24.377	39.192	32.5	6.9042	3.9452	32.5	1.75003	2.9407	48.6363	45.7715	79.1504	115.1233	0.2593	20.3035
	24.377	39.192	35	7.5219	4.2982	35	1.75001	3.1282	61.4073	57.7929	99.9356	145.3585	0.2707	23.5304
	24.377	39.192	37.5	7.7097	4.4056	37.5	1.74998	3.1904	65.7897	61.9244	107.0723	155.7481	0.2736	24.5974
RHo 6	24.377	39.192	40	7.6089	4.348	40	1.74998	3.1568	63.4043	59.6792	103.1900	150.1010	0.2721	24.0196
	24.666	39.04	2.5	5.5158	3.152	2.5	1.74994	2.6209	27.6607	26.0391	45.0199	65.4908	0.2371	14.4564
	24.666	39.04	5	5.8186	3.3249	5	1.75001	2.6789	31.4670	29.6153	51.2104	74.4872	0.2402	15.5875
	24.666	39.04	7.5	5.9782	3.4161	7.5	1.75001	2.7120	33.6271	31.6483	54.7258	79.6005	0.2424	16.2129
	24.666	39.04	10	6.1985	3.542	10	1.75000	2.7607	36.7992	34.6346	59.8887	87.1112	0.2459	17.1119
	24.666	39.04	12.5	6.2933	3.5962	12.5	1.74999	2.7827	38.2351	35.9876	62.2266	90.5138	0.2475	17.5123
	24.666	39.04	15	6.1608	3.5205	15	1.74998	2.7521	36.2383	34.1091	58.9775	85.7888	0.2453	16.9550
	24.666	39.04	17.5	6.4936	3.7105	17.5	1.75006	2.8314	41.4275	38.9828	67.4158	98.0496	0.2513	18.3863
	24.666	39.04	20	6.4367	3.6781	20	1.75001	2.8173	40.4965	38.1135	65.9052	95.8614	0.2502	18.1341
	24.666	39.04	22.5	6.2562	3.575	22.5	1.74999	2.7740	37.6674	35.4533	61.3027	89.1701	0.2469	17.3546
	24.666	39.04	25	6.4651	3.6944	25	1.74997	2.8243	40.9537	38.5481	66.6521	96.9533	0.2507	18.2595
RHo 7	24.666	39.04	27.5	6.601	3.772	27.5	1.75000	2.8588	43.2175	40.6753	70.3340	102.3044	0.2533	18.8711
	24.666	39.04	30	6.5697	3.7541	30	1.75001	2.8508	42.6884	40.1764	69.4724	101.0500	0.2527	18.7286
	24.666	39.04	32.5	7.4126	4.2357	32.5	1.75003	3.0931	58.9685	55.4943	95.9643	139.5780	0.2689	22.9281
	24.666	39.04	35	7.6028	4.3444	35	1.75002	3.1548	63.2685	59.5423	102.9630	149.7591	0.2720	23.9850
	24.666	39.04	37.5	7.7012	4.4007	37.5	1.74999	3.1876	65.5882	61.7312	106.7420	155.2631	0.2735	24.5482
	24.666	39.04	40	7.7873	4.45	40	1.74996	3.2168	67.6723	63.7010	110.1391	160.2152	0.2747	25.0503
	24.71	39.543	2.5	5.4956	3.1404	2.5	1.74997	2.6173	27.4220	25.8117	44.6296	64.9196	0.2369	14.3834
	24.71	39.543	5	6.1924	3.5385	5	1.75001	2.7593	36.7088	34.5487	59.7410	86.8954	0.2458	17.0865
	24.71	39.543	7.5	6.0157	3.4375	7.5	1.75002	2.7200	34.1523	32.1410	55.5794	80.8401	0.2429	16.3629
	24.71	39.543	10	6.0196	3.4397	10	1.75004	2.7209	34.2082	32.1921	55.6694	80.9690	0.2430	16.3786
	24.71	39.543	12.5	6.1171	3.4955	12.5	1.74999	2.7423	35.5998	33.5064	57.9372	84.2736	0.2445	16.7747
RHo 8	24.71	39.543	15	6.1575	3.5187	15	1.74994	2.7513	36.1864	34.0649	58.8961	85.6767	0.2452	16.9413
	24.71	39.543	17.5	6.0993	3.4853	17.5	1.75001	2.7383	35.3429	33.2631	57.5181	83.6620	0.2442	16.7018

	24.71	39.543	20	6.3125	3.6071	20	1.75002	2.7872	38.5344	36.2652	62.7110	91.2131	0.2479	17.5944
	24.71	39.543	22.5	6.1418	3.5096	22.5	1.75000	2.7478	35.9607	33.8454	58.5241	85.1263	0.2449	16.8764
	24.71	39.543	25	6.5971	3.7698	25	1.74999	2.8578	43.1499	40.6135	70.2253	102.1486	0.2532	18.8533
	24.71	39.543	27.5	6.7617	3.8638	27.5	1.75001	2.9014	46.0239	43.3147	74.9001	108.9436	0.2565	19.6183
	24.71	39.543	30	6.7296	3.8454	30	1.75004	2.8927	45.4544	42.7752	73.9709	107.5874	0.2559	19.4669
	24.71	39.543	32.5	7.0242	4.0138	32.5	1.75001	2.9750	50.9274	47.9297	82.8802	120.5510	0.2617	20.8973
	24.71	39.543	35	7.5902	4.3372	35	1.75002	3.1506	62.9759	59.2669	102.4868	149.0664	0.2718	23.9137
	24.71	39.543	37.5	7.9278	4.5302	37.5	1.74999	3.2655	71.2032	67.0172	115.8809	168.5578	0.2763	25.8883
	24.71	39.543	40	7.8241	4.471	40	1.74997	3.2295	68.5834	64.5562	111.6204	162.3669	0.2751	25.2675
	24.785	39.915	2.5	5.1239	2.928	2.5	1.74997	2.5542	23.2634	21.8974	37.8615	55.0747	0.2357	13.0873
	24.785	39.915	5	5.862	3.3497	5	1.75001	2.6877	32.0433	30.1577	52.1483	75.8514	0.2407	15.7555
	24.785	39.915	7.5	6.1775	3.5299	7.5	1.75005	2.7559	36.4908	34.3386	59.3829	86.3683	0.2455	17.0244
	24.785	39.915	10	5.9486	3.3991	10	1.75005	2.7057	33.2211	31.2616	54.0620	78.6291	0.2419	16.0953
	24.785	39.915	12.5	6.1439	3.5109	12.5	1.74995	2.7483	35.9877	33.8763	58.5716	85.2026	0.2450	16.8851
	24.785	39.915	15	6.1517	3.5153	15	1.74998	2.7500	36.1044	33.9830	58.7595	85.4717	0.2451	16.9173
	24.785	39.915	17.5	6.3049	3.6027	17.5	1.75005	2.7854	38.4191	36.1534	62.5211	90.9327	0.2478	17.5619
	24.785	39.915	20	6.3265	3.6151	20	1.75002	2.7906	38.7518	36.4698	63.0647	91.7276	0.2481	17.6545
	24.785	39.915	22.5	6.2237	3.5564	22.5	1.75000	2.7664	37.1769	34.9900	60.5033	88.0052	0.2463	17.2176
	24.785	39.915	25	6.4664	3.6951	25	1.74999	2.8246	40.9766	38.5671	66.6877	97.0018	0.2507	18.2653
	24.785	39.915	27.5	6.4537	3.6878	27.5	1.75001	2.8215	40.7720	38.3719	66.3531	96.5117	0.2505	18.2091
RH09	24.785	39.915	30	6.6577	3.8043	30	1.75005	2.8736	44.1951	41.5890	71.9208	104.6043	0.2544	19.1317
	24.785	39.915	32.5	6.8318	3.9038	32.5	1.75004	2.9206	47.2961	44.5084	76.9681	111.9467	0.2579	19.9527
	24.785	39.915	35	7.799	4.4565	35	1.75003	3.2208	67.9710	63.9668	110.6151	160.8877	0.2748	25.1192
	24.785	39.915	37.5	8.2863	4.735	37.5	1.75001	3.3951	80.8793	76.1190	131.6248	191.4516	0.2792	28.1329
	24.785	39.915	40	8.2022	4.687	40	1.74999	3.3640	78.5173	73.9012	127.7842	185.8720	0.2787	27.5926
	24.916	39.691	2.5	4.9518	2.8296	2.5	1.75000	2.5274	21.5005	20.2358	34.9910	50.8961	0.2362	12.5151
	24.916	39.691	5	6.286	3.592	5	1.75000	2.7810	38.1240	35.8814	62.0447	90.2471	0.2474	17.4812
	24.916	39.691	7.5	6.403	3.6588	7.5	1.75003	2.8090	39.9577	37.6039	65.0267	94.5803	0.2495	17.9862
	24.916	39.691	10	6.1567	3.5181	10	1.75001	2.7512	36.1801	34.0511	58.8806	85.6439	0.2452	16.9380
	24.916	39.691	12.5	5.9664	3.4094	12.5	1.74999	2.7095	33.4620	31.4951	54.4585	79.2147	0.2422	16.1659
	24.916	39.691	15	6.1366	3.5067	15	1.74996	2.7466	35.8819	33.7751	58.3984	84.9486	0.2449	16.8550
	24.916	39.691	17.5	6.3401	3.6229	17.5	1.75001	2.7938	38.9627	36.6700	63.4091	92.2307	0.2484	17.7131
	24.916	39.691	20	6.2831	3.5903	20	1.75002	2.7803	38.0812	35.8386	61.9733	90.1402	0.2474	17.4688
	24.916	39.691	22.5	6.3088	3.6051	22.5	1.74997	2.7864	38.4725	36.2136	62.6147	91.0816	0.2478	17.5786
	24.916	39.691	25	6.5349	3.7343	25	1.74997	2.8419	42.1021	39.6299	68.5217	99.6740	0.2520	18.5713
	24.916	39.691	27.5	6.6338	3.7908	27.5	1.74997	2.8674	43.7758	41.2043	71.2451	103.6343	0.2540	19.0214
RH11	24.916	39.691	30	6.77	3.8685	30	1.75003	2.9036	46.1746	43.4539	75.1436	109.2942	0.2567	19.6577
	24.916	39.691	32.5	6.9679	3.9816	32.5	1.75003	2.9588	49.8424	46.9066	81.1131	117.9782	0.2606	20.6168
RH13	24.916	39.691	35	7.4854	4.2774	35	1.74999	3.1164	60.5800	57.0187	98.5921	143.4102	0.2701	23.3277
	24.916	39.691	37.5	7.8932	4.5104	37.5	1.75000	3.2534	70.3230	66.1864	114.4468	166.4688	0.2760	25.6798
	24.916	39.691	40	7.9565	4.5466	40	1.74999	3.2756	71.9414	67.7120	117.0823	170.3053	0.2767	26.0624
	24.916	39.691	42.5	8.0438	4.453	42.5	1.80638	3.3066	82.8121	65.5678	126.5236	167.7295	0.2775	26.5978
	24.208	39.365	2.5	5.0814	2.9037	2.5	1.74997	2.5474	22.8191	21.4786	37.1380	54.0215	0.2358	12.9445

RH14	24.208	39.365	5	5.9347	3.3912	5	1.75003	2.7028	33.0288	31.0829	53.7505	78.1789	0.2417	16.0403
	24.208	39.365	7.5	6.047	3.4554	7.5	1.75001	2.7268	34.5941	32.5576	56.2990	81.8877	0.2434	16.4891
	24.208	39.365	10	6.0094	3.4339	10	1.75002	2.7187	34.0638	32.0577	55.4354	80.6306	0.2428	16.3376
	24.208	39.365	12.5	6.1314	3.5037	12.5	1.74998	2.7455	35.8070	33.7031	58.2755	84.7677	0.2448	16.8335
	24.208	39.365	15	6.4481	3.6847	15	1.74997	2.8201	40.6771	38.2886	66.2026	96.3006	0.2504	18.1843
	24.208	39.365	17.5	6.1434	3.5104	17.5	1.75006	2.7482	35.9886	33.8653	58.5652	85.1779	0.2450	16.8830
	24.208	39.365	20	6.532	3.7325	20	1.75003	2.8411	42.0599	39.5814	68.4472	99.5543	0.2520	18.5583
	24.208	39.365	22.5	6.4826	3.7044	22.5	1.74997	2.8287	41.2393	38.8169	67.1170	97.6296	0.2510	18.3373
	24.208	39.365	25	6.7162	3.8379	25	1.74997	2.8891	45.2104	42.5556	73.5805	107.0325	0.2556	19.4041
	24.208	39.365	27.5	6.893	3.9389	27.5	1.74998	2.9376	48.4221	45.5766	78.8063	114.6314	0.2591	20.2489
	24.208	39.365	30	6.8198	3.8969	30	1.75006	2.9173	47.0787	44.3009	76.6124	111.4257	0.2576	19.8951
	24.208	39.365	32.5	6.9897	3.994	32.5	1.75005	2.9651	50.2635	47.2990	81.7958	118.9661	0.2610	20.7250
	24.208	39.365	35	7.2442	4.1395	35	1.75002	3.0406	55.3622	52.1025	90.0969	131.0464	0.2659	22.0269
	24.208	39.365	37.5	7.7864	4.4494	37.5	1.74999	3.2165	67.6550	63.6777	110.1064	160.1585	0.2746	25.0450
	24.208	39.365	40	7.6961	4.3978	40	1.74999	3.1859	65.4653	61.6167	106.5427	154.9748	0.2734	24.5187
	24.386	39.757	2.5	5.1934	2.9677	2.5	1.74997	2.5654	24.0042	22.5941	39.0668	56.8270	0.2357	13.3231
	24.386	39.757	5	5.8363	3.335	5	1.75001	2.6825	31.7016	29.8353	51.5916	75.0407	0.2404	15.6559
	24.386	39.757	7.5	6.151	3.5148	7.5	1.75003	2.7499	36.0979	33.9714	58.7453	85.4439	0.2451	16.9144
	24.386	39.757	10	5.9825	3.4185	10	1.75004	2.7129	33.6890	31.7035	54.8245	79.7400	0.2424	16.2300
	24.386	39.757	12.5	6.2615	3.578	12.5	1.75000	2.7752	37.7492	35.5287	61.4348	89.3600	0.2470	17.3771
	24.386	39.757	15	6.0292	3.4453	15	1.74998	2.7229	34.3393	32.3217	55.8869	81.2933	0.2431	16.4172
	24.386	39.757	17.5	6.3021	3.6011	17.5	1.75005	2.7848	38.3759	36.1127	62.4508	90.8303	0.2477	17.5499
	24.386	39.757	20	6.1057	3.4889	20	1.75004	2.7397	35.4377	33.3491	57.6702	83.8791	0.2443	16.7280
	24.386	39.757	22.5	6.388	3.6503	22.5	1.74999	2.8054	39.7161	37.3807	64.6363	94.0178	0.2493	17.9207
	24.386	39.757	25	6.6444	3.7969	25	1.74995	2.8701	43.9564	41.3771	71.5409	104.0680	0.2542	19.0703
	24.386	39.757	27.5	6.8381	3.9075	27.5	1.74999	2.9223	47.4071	44.6194	77.1530	112.2242	0.2580	19.9830
	24.386	39.757	30	6.7474	3.8556	30	1.75003	2.8975	45.7696	43.0736	74.4851	108.3376	0.2562	19.5508
	24.386	39.757	32.5	6.9764	3.9865	32.5	1.75001	2.9613	50.0031	47.0608	81.3767	118.3653	0.2607	20.6589
	24.386	39.757	35	7.3112	4.1778	35	1.75001	3.0613	56.7733	53.4316	92.3940	134.3891	0.2671	22.3816
	24.386	39.757	37.5	7.9916	4.5666	37.5	1.75001	3.2880	72.8561	68.5679	118.5676	172.4594	0.2770	26.2766
	24.386	39.757	40	8.1105	4.6346	40	1.74999	3.3306	76.0088	71.5403	123.7019	179.9340	0.2781	27.0130
RH15	24.173	39.839	2.5	5.433	3.1046	2.5	1.74998	2.6061	26.6873	25.1188	43.4330	63.1772	0.2365	14.1588
	24.173	39.839	5	5.8207	3.3261	5	1.75001	2.6793	31.4947	29.6414	51.2555	74.5527	0.2402	15.5956
	24.173	39.839	7.5	6.0836	3.4763	7.5	1.75002	2.7348	35.1177	33.0496	57.1505	83.1253	0.2440	16.6377
	24.173	39.839	10	5.9549	3.4028	10	1.75000	2.7071	33.3042	31.3451	54.2007	78.8377	0.2420	16.1202
	24.173	39.839	12.5	6.0276	3.4444	12.5	1.74997	2.7226	34.3162	32.3007	55.8497	81.2403	0.2431	16.4108
	24.173	39.839	15	6.2275	3.5586	15	1.74999	2.7673	37.2330	35.0444	60.5957	88.1416	0.2464	17.2335
	24.173	39.839	17.5	6.3396	3.6226	17.5	1.75001	2.7937	38.9555	36.6623	63.3968	92.2117	0.2484	17.7109
	24.173	39.839	20	6.4545	3.6882	20	1.75004	2.8217	40.7874	38.3830	66.3758	96.5403	0.2505	18.2126
	24.173	39.839	22.5	6.5123	3.7214	22.5	1.74996	2.8361	41.7266	39.2773	67.9112	98.7871	0.2516	18.4699
	24.173	39.839	25	6.4968	3.7125	25	1.74998	2.8322	41.4729	39.0359	67.4966	98.1806	0.2513	18.4005
	24.173	39.839	27.5	6.6146	3.7798	27.5	1.74999	2.8623	43.4480	40.8941	70.7105	102.8543	0.2536	18.9333
	24.173	39.839	30	6.8023	3.887	30	1.75001	2.9125	46.7558	44.0035	76.0912	110.6761	0.2573	19.8114

	24.173	39.839	32.5	6.9219	3.9554	32.5	1.74999	2.9457	48.9650	46.0866	79.6891	115.9144	0.2597	20.3901
	24.173	39.839	35	7.0574	4.0328	35	1.75000	2.9847	51.5757	48.5419	83.9367	122.0902	0.2623	21.0643
	24.173	39.839	37.5	7.7692	4.4396	37.5	1.74998	3.2106	67.2318	63.2817	109.4192	159.1618	0.2744	24.9440
	24.173	39.839	40	8.0257	4.5862	40	1.74997	3.3002	73.7434	69.4130	120.0182	174.5823	0.2773	26.4861

Table 2: The average elastic constants for upper and lower crust in the 13 seismic broadband stations around Northern Harrat Rahat (REF data source: Tang et al., 2019). Abbreviations are: P-wave velocity, V_P; Shear-wave velocity, V_S; Density (g/cm^3), ρ; Lame's Second constant (Shear Modulus), μ; Lame's First constant, λ; Bulk Modulus, K; Young's Modulus, E; and Poisson Ratio, σ; Acoustic impedance, AI; Thickness of upper crust, h_{UC}; thickness of lower crust, h_{LC}.

Station	Latitude	Longitude	Moho(km)	huc	Vp	Vs	Vp/Vs	ρ	λ	μ	K	Bulk Compression (1/K)	E	σ	AI
Upper crust															
RH01	24.27	39.81	34.40	7.50	6.020	3.530	1.705	2.707	30.639	33.732	53.127	0.019	83.519	0.238	16.296
RH02	24.48	40.09	34.80	15.00	6.290	3.680	1.709	2.789	34.805	37.770	59.985	0.017	93.653	0.240	17.543
RH03	24.25	40.17	35.80	15.00	6.240	3.650	1.710	2.771	34.063	36.917	58.674	0.017	91.549	0.240	17.291
RH04	23.99	39.88	35.40	10.00	6.020	3.680	1.636	2.707	24.784	36.659	49.224	0.020	88.106	0.202	16.296
RH05	23.91	39.16	27.20	12.50	6.270	3.660	1.713	2.778	34.785	37.213	59.594	0.017	92.405	0.242	17.418
RH06	24.38	39.19	34.00	10.00	6.290	3.620	1.738	2.760	36.861	36.168	60.973	0.016	90.592	0.252	17.360
RH07	24.67	39.04	32.40	10.00	6.220	3.640	1.709	2.766	33.715	36.648	58.148	0.017	90.857	0.240	17.205
RH08	24.71	39.54	34.80	12.50	6.290	3.670	1.714	2.783	35.139	37.484	60.128	0.017	93.105	0.242	17.505
RH09	24.78	39.91	35.00	12.50	6.130	3.570	1.717	2.748	33.215	35.023	56.564	0.018	87.094	0.243	16.845
RH10	24.58	39.90	34.60	10.00	6.220	3.640	1.709	2.766	33.715	36.648	58.148	0.017	90.857	0.240	17.205
RH11	24.92	39.69	35.40	15.00	6.240	3.650	1.710	2.771	34.063	36.917	58.674	0.017	91.549	0.240	17.291
RH13	24.21	39.37	36.10	12.50	6.060	3.560	1.702	2.731	31.069	34.612	54.143	0.018	85.596	0.237	16.550
RH14	24.39	39.76	35.80	12.50	5.884	3.362	1.750	2.653	31.877	29.987	51.868	0.019	75.425	0.258	15.610
RH15	24.17	39.84	35.70	12.50	5.863	3.350	1.750	2.646	31.566	29.695	51.363	0.019	74.690	0.258	15.513
Lower crust															
Station	Latitude	Longitude	Moho (km)	h_{LC}	Vp	Vs	Vp/Vs	ρ	λ	μ	K	Bulk Compression (1/K)	E	σ	AI
RH01	24.27	39.81	34.40	26.90	7.273	3.910	1.860	3.049	68.045	46.619	99.124	0.010	120.902	0.297	22.177
RH02	24.48	40.09	34.80	19.80	6.974	3.940	1.770	2.961	52.066	45.958	82.704	0.012	116.326	0.266	20.646
RH03	24.25	40.17	35.80	20.80	6.747	3.900	1.730	2.897	43.757	44.070	73.137	0.014	110.096	0.249	19.549
RH04	23.99	39.88	35.40	25.40	6.938	3.920	1.770	2.950	51.363	45.337	81.587	0.012	114.756	0.266	20.471
RH05	23.91	39.16	27.20	14.70	6.940	4.010	1.731	2.951	47.224	47.450	78.857	0.013	118.569	0.249	20.479
RH06	24.38	39.19	34.00	24.00	6.810	3.940	1.728	2.915	44.677	45.244	74.840	0.013	112.968	0.248	19.848
RH07	24.67	39.04	32.40	22.40	6.669	3.900	1.710	2.877	40.432	43.753	69.601	0.014	108.520	0.240	19.184
RH08	24.71	39.54	34.80	22.30	6.829	3.880	1.760	2.920	48.245	43.955	77.548	0.013	110.910	0.262	19.938
RH09	24.78	39.91	35.00	22.50	6.755	3.860	1.750	2.900	45.903	43.203	74.704	0.013	108.661	0.258	19.587
RH10	24.58	39.90	34.60	24.60	6.906	3.880	1.780	2.941	51.737	44.280	81.258	0.012	112.421	0.269	20.314
RH11	24.92	39.69	35.40	20.40	6.730	3.890	1.730	2.893	43.463	43.774	72.645	0.014	109.356	0.249	19.467
RH13	24.21	39.37	36.10	23.60	7.000	4.030	1.737	2.968	49.027	48.204	81.163	0.012	120.713	0.252	20.776
RH14	24.39	39.76	35.80	23.30	6.771	3.847	1.760	2.904	47.169	42.975	75.820	0.013	108.438	0.262	19.661
RH15	24.17	39.84	35.70	23.20	6.910	3.839	1.800	2.942	53.773	43.365	82.683	0.012	110.737	0.277	20.333

Table 3: Hydraulic parameters were estimated from the pumping test data from the boreholes drilled to shallow depths in the Madinah Basaltic Terrain, Northern Harrat Rahat. Source: Al-Shaibani (2003).

Well no	Transmissivity (m^2/s)	Specific Yield	Remarks
ME-T1	$3x10^{-3}$	$8.7x10^{-2}$	Italconsult (1979)
ME-T2	$3.2x10^{-3}$	$2.6x10^{-4}$	Italconsult (1979)
ME-T5	$2.5x10^{-2}$	-	Italconsult (1979)
WSA-301	$2.1x10^{-3}$	-	By driller, reported in Al-Shaibani (2003)
WSA-302	$5.5x10^{-5}$	-	Permeability is locally very low
WSA-303	$9.8x10^{-3}$	-	-
WSA-306	0.15	-	Productive well, highly fractured zone?
WSA-328	$7.0x10^{-2}$	$8.5x10^{-2}$	Al-Shaibani (2003)
BR-14	$1.8x10^{-4}$	$4x10^{-2}$	Reported in Al-Shaibani (2003)